Rock Mechanics and Rock Engineering
https://doi.org/10.1007/s00603-024-03802-z

ORIGINAL PAPER

Deformation Behavior and Seismic Characteristics of Sandy Facies Opalinus Clay During Triaxial Deformation Under Dry and Wet Conditions

Valerian Schuster[1] · **Erik Rybacki**[1] · **Audrey Bonnelye**[1,2] · **Georg Dresen**[1,3]

Received: 25 July 2023 / Accepted: 25 January 2024

Abstract

Unconsolidated, undrained triaxial deformation tests were performed on sandy facies Opalinus Clay at 50 MPa confining pressure to characterize the effect of water and microfabric orientation on the deformation behavior, mechanical properties, and P-wave velocity evolution. Dry and wet (≈ 8 and $> 95\%$ initial water saturation, respectively) samples with 12.6 ± 0.4 vol% porosity were deformed parallel and perpendicular to the bedding direction at a constant strain rate of 5×10^{-6} s^{-1}. Dry samples revealed semi-brittle behavior and exhibited strain localization at failure, while deformation was more ductile at saturated conditions, promoting stable, slow faulting. Peak strength, Young's modulus, and number of cumulative acoustic emissions decreased significantly for wet samples compared to dry samples; the opposite was observed for Poisson's ratio. P-wave velocity anisotropy was significantly altered by differential stress, primarily due to the interplay between pore and fracture closure and stress-induced microcrack formation. For samples that were deformed perpendicular to bedding, we observed a reduction and reversal of P-wave velocity anisotropy with increasing differential stress, whereas anisotropy of parallel samples increased. The results suggest that water saturation reduces the pressure at the brittle-ductile transition and that the elastic properties and anisotropy of sandy facies Opalinus Clay can be significantly altered in an anisotropic stress field, e.g., adjacent to fault zones or tunnel excavations. Changes in elastic anisotropy are primarily controlled by the orientation between the pre-existing microfabric and the maximum principal stress direction, stress magnitude, and the degree of water saturation.

Highlights

- The presence of water reduces compressive strength, stiffness and P-wave velocity anisotropy of sandy facies Opalinus Clay, accompanied by increasing strain delocalization, promoting stable, slow faulting during triaxial deformation
- Triaxial deformation alters the elastic wave velocity anisotropy and symmetry of sandy facies Opalinus Clay, depending on water content and on the orientation of bedding relative to loading direction
- Changes in elastic anisotropy are mainly controlled by the closure of pores and microcracks and the formation of stress-induced fractures

Keywords Opalinus Clay · Triaxial deformation · Geomechanics · P-wave velocity anisotropy · Microstructures

✉ Valerian Schuster
valerian.schuster@gfz-potsdam.de

[1] Helmholtz Centre Potsdam, GFZ German Research Centre for Geosciences, 14473 Potsdam, Germany

[2] GeoRessources Laboratory, Université de Lorraine, 54000 Nancy, France

[3] Institute for Earth and Environmental Science, University of Potsdam, 14476 Potsdam, Germany

Published online: 16 March 2024

Abbreviations

A_p	Anisotropy coefficient
c_d	Stress at the onset of net dilation
c_i	Stress at the onset of microcracking
D_{tot}	Total axial shortening of the specimen
E	Young's modulus
L	Sample length
p_c	Confining pressure
p_f	Pore pressure
α	Effective stress coefficient
β	Angle between wave propagation and sample axis normal
ε_{ax}	Axial strain
ε_{rad}	Radial strain
ε_{tot}	Total axial strain
ε_{vol}	Volumetric strain
θ	Angle between wave propagation and bedding normal
ν	Poisson's ratio
σ_1	Maximum principal stress
σ_{diff}	Differential stress
σ_{max}	Peak (differential) strength
σ_{mean}'	Effective mean stress
σ_{mean}	Total mean stress
σ_n'	Effective normal stress
σ_n	Normal stress

1 Introduction

Clay-dominated sedimentary rocks, such as the Jurassic Opalinus Clay (OPA) formation, are considered to be effective natural barriers for fluid migration due to their low hydraulic conductivity and high self-sealing capacity (Philipp et al. 2017; Zhang and Talandier 2022). Therefore, these rock types play a fundamental role in many geo-engineering applications, as they represent suitable caprock seals of reservoir formations, e.g., for carbon dioxide sequestration (Bossart et al. 2017; Zappone et al. 2021), hydrocarbon extraction, or potential host rocks for the deep geological storage of nuclear waste (NAGRA 2002).

However, the excavation of underground galleries or the exploitation of deep reservoirs leads to effective stress changes that can cause rock damage or failure and thus an alteration of the mechanical and hydraulic properties of the sealing units, affecting their barrier integrity (e.g., Ingram and Urai 1999; Bossart et al. 2002; Lisjak et al. 2015). The extent of sealing loss depends on the type of deformation/failure mode induced by stress changes, i.e., essentially the contribution of brittle, dilatant mechanisms (e.g., cataclasis) leading to localized deformation and an increase in porosity as a consequence of rock decompaction. In general, three types of deformation mechanisms are distinguished in rock deformation: brittle, semi-brittle and plastic, whereby the transition between failure modes for individual rocks is significantly controlled by the acting confining pressure, temperature, strain rate and water content (e.g., Evans et al. 1990). Understanding the processes that act during diffuse (ductile) or localized (brittle) rock failure and how they modify essential rock properties such as strength and elasticity is a prerequisite for predicting long-term evolution of geo-engineering systems at (sub-) critical stress conditions.

The in-situ behavior of OPA has been studied for more than 20 years at the Mont Terri Underground Research Laboratory (MT URL, Switzerland; Bossart et al. 2017), as the formation is the envisaged host rock for the disposal of nuclear waste in Switzerland (NAGRA 2002, 2022) and is being considered as part of the site selection process in Germany (Hoth et al. 2007; BGE 2022). Several sub-facies types were identified at the MT URL, which can simplified be subdivided into a carbonate-rich sandy, sandy and shaly lithofacies type (Thury and Bossart 1999; Pearson et al. 2003; Hostettler et al. 2017; Lauper et al. 2018, 2021; Kneuker and Furche 2021), whereas laboratory characterization of hydromechanical and microstructural properties of OPA predominantly focused on the homogeneous, clay-rich shaly facies (e.g., Amann et al. 2011; Wild et al. 2015; Favero et al. 2018; Giger et al. 2018; Wild and Amann 2018; Minardi et al. 2020; Winhausen et al. 2022, 2023). The deformation behavior of clay-rich rocks is determined by their mineralogical composition (e.g., Bourg 2015), diagenesis and burial history/consolidation state (Gutierrez et al. 1996; Nygård et al. 2004; Crisci et al. 2019). In the case of OPA, laboratory studies reveal that the quartz-rich sandy facies displays a higher mechanical strength and stiffness in comparison to the clay mineral-dominated shaly facies (e.g., Nüesch 1991; Schuster et al. 2021), whereby decreasing clay mineral content favors brittle, dilatant deformation. As for many other clay-rich sedimentary rocks (e.g., Vernik and Liu 1997; Dewhurst and Siggins 2006; Sarout and Guéguen 2008; Delle Piane et al. 2011; Bonnelye et al. 2017; Zhang et al. 2019), the microstructural fabric of OPA is characterized by a preferred textural orientation and alignment of clay minerals as well as low-aspect ratio microcracks and pores (e.g., Wenk et al. 2008; Houben et al. 2013, 2014), which results in a pronounced anisotropy of mechanical strength, hydraulic properties as well as static and dynamic elastic stiffness (e.g., Popp and Salzer 2007; Sarout et al. 2014a, b; Siegesmund et al. 2014; Wild and Amann 2018; Yurikov et al. 2019; Schuster et al 2021; Wenning et al. 2021), thus significantly affecting the deformation behavior.

Previous experimental studies have shown that the deformation behavior of OPA and other shales and soils is strongly influenced by water content and applied confining pressure, with brittle failure being favored at both, low

confinement and/or water saturation, while decreasing water saturation further increases strength and stiffness (Nüesch 1991; Cui and Delage 1996; Chiarelli et al. 2000; Valès et al. 2004; Zhang et al. 2012; Giger and Marschall 2014; Wild et al. 2015; Zhang et al. 2019; Douma et al. 2019; Schuster et al. 2021, 2023; Winhausen et al. 2022). At microscale, the deformation behavior of OPA in the laboratory is characterized by a coexistence of brittle (microfracturing, particle sliding) and crystal plastic (bending, kinking) mechanisms, where the contribution of each mechanism was found to be highly dependent on confining pressure, bedding orientation and mineral composition (Nüesch 1991; Schuster et al. 2021, 2022; Winhausen et al. 2022, 2023). In agreement with the bulk mechanical response derived from stress–strain curves, the relative contribution of dilatant micro-cracking and rigid grain rotation decreases with increasing confining pressure (Schuster et al. 2021, 2023; Winhausen et al. 2022, 2023), whereas bending of phyllosilicates as well as frictional sliding become more important mechanisms, resulting in increased ductility.

In general, the presence of water has a weakening effect on the brittle strength of rocks, while its influence on the deformation behavior is primarily driven by a combination of hydromechanical and physico-chemical effects that depend on the rock type and its characteristics such as mineralogy as well as poroelastic and hydraulic properties (e.g., Van Eeckhout 1976; Baud et al. 2000; Paterson and Wong 2005; Jaeger et al. 2007; Scholz 2019).

Hydromechanical effects of water are related to an increase of pore fluid pressure (p_f), which lowers the bulk strength of a rock due to a reduction of effective normal stress (σ_n') according to the effective stress law $\sigma_n' = \sigma_n - \alpha p_f$, where α is the effective stress coefficient (e.g., Terzaghi 1936; Brace and Martin 1968; Paterson and Wong 2005; Jaeger et al. 2007). During deformation under effectively undrained conditions (e.g., due to an increase in mean stress), compaction due to pore volume reduction can further increase pore pressure, whereas brittle faulting, e.g., microcrack nucleation and propagation, can lead to dilation and therefore a reduction in pore pressure (e.g., John et al. 1963; Brace and Martin 1968; Bernabé and Brace 1990; Ibanez and Kronenberg 1993; Wild and Amann 2018). The degree of dilation in a water-saturated rock depends on its hydraulic diffusivity and the timescale of the applied deformation. If dilation due to microcracking occurs at a faster rate than pore fluids can diffuse into the newly created void space (deformation above a critical strain rate; Brace and Martin 1968), pore pressure will drop locally, stabilizing further crack growth and failure due to increasing effective normal stress, which results in higher strength, also known as dilatancy hardening (e.g., Rice 1975; Duda and Renner 2012; Faulkner et al. 2018; Brantut 2021). Conversely, if the applied strain rate allows equilibration of pore pressure, deformation is locally drained, reducing the strengthening effect by dilatant hardening.

Physico-chemical water weakening effects are related to crack lubrication and a reduction of friction coefficient (e.g., Van Eeckhout 1976; Lockner 1998) as well as time-dependent subcritical crack growth phenomena (e.g., Atkinson 1984; Heap et al. 2009; Brantut et al. 2013), controlled by the decrease of free surface energy (e.g., Rehbinder and Lichtman 1957) and water-assisted stress corrosion (e.g., Scholz 1972; Anderson and Grew 1977; Kranz et al. 1982), which is especially important for silicate-rich rocks. The strengthening of clay-dominated rocks and soils resulting from to the removal of interlayer and surface-adsorbed water is frequently attributed to an increase in frictional, osmotic and capillary suction forces, resulting in an additional compression between mineral grains, which in turn enhances their shear resistance (Hawkins and McConnell 1992; Schmitt et al. 1994; Saffer and Marone 2003; Moore and Lockner 2004; Valès et al. 2004; Ikari et al. 2007, 2009; Ramos da Silva et al. 2008; Ghorbani et al. 2009; Morrow et al. 2017). On the other hand, desaturation of shales causes shrinkage and the formation of desiccation microcracks (Pham et al. 2007; Soe et al. 2009; Houben et al. 2013; Minardi et al. 2016).

In this study, we present a set of triaxial deformation experiments performed on dry or water-saturated samples of the sandy facies of OPA, combined with monitoring of ultrasonic P-wave velocities along several ray paths as well as of acoustic emission (AE) events with subsequent electron microscopy of deformed samples. To this end, cylindrical samples of the sandy facies were prepared parallel and perpendicular to bedding, and deformed at an elevated confining pressure of 50 MPa. At this pressure, the sandy facies of OPA deforms in the semi-brittle regime (combination of brittle and plastic mechanisms), whereas deformation becomes increasingly ductile (non-localized) at high water saturation (Schuster et al. 2021). P-wave velocities are sensitive to the dynamic rock stiffness and can therefore resolve structural elastic anisotropy, e.g., induced by a preferred fabric orientation of mineral phases, pre-existing fault zones or sedimentary bedding planes, stress-induced formation/opening or closure of oriented crack networks in a heterogeneous stress field on a regional scale, or by application of a differential stress in the laboratory (e.g., Crampin et al. 1984; Sayers and Kachanov 1995; Boness and Zoback 2006; Dewhurst and Siggins 2006; Fortin et al. 2006; Delle Piane et al. 2011). Brittle inelastic deformation, e.g., microcracking can radiate high-frequency elastic waves (AE events) that can be used to describe spatio-temporal evolution of damage and rupture of fractures during the deformation of rock or rock-like materials like concrete (e.g., Scholz 1968; Grosse et al. 1997; Lockner 1993). Accordingly, there exists a plethora of studies using AE monitoring to describe failure mechanisms of intact rocks from nucleation of

individual cracks to coalescence and fracture formation as well as of simulated faults by analyzing hypocenter location, source mechanisms (i.e., tensile, shear, compaction), frequency and magnitude distributions as well as amplitudes of recorded AE events and their statistics (e.g., Zang et al. 1998; Fortin et al. 2006; Thompson et al. 2009; Amann et al. 2011; Carpinteri et al. 2013, 2016; Goebel et al. 2012; Kwiatek et al. 2014). The anisotropy of mechanical, seismic and hydraulic parameters must be considered for an improved prediction of the hydro-mechanical response of the rock mass and induced damage during and after gallery construction (e.g., Bossart et al. 2002; Winhausen et al. 2023), but also for in-situ geophysical underground exploration techniques such as seismic tomography, which can be used for the detection of heterogeneities (e.g., rock composition) or pre-existing tectonic structures (Nicollin et al. 2008; Schuster et al. 2017; Esefelder et al. 2021; Zappone et al. 2021; Wawerzinek et al. 2022; Williams et al. 2022). To date only few studies have characterized the physical processes and micromechanics that govern the anisotropic deformation of OPA using ultrasonic monitoring or BIB (broad ion beam) polishing for high resolution scanning electron microscopy (SEM) imaging of deformation structures (Popp and Salzer 2007; Sarout et al. 2014a, b; Siegesmund et al. 2014; Lozovyi and Bauer 2019; Schuster et al. 2021, 2023; Winhausen et al. 2022, 2023). Measuring the evolution of P-wave velocities at different angles with respect to the bedding allows to study changes in the dynamic elastic anisotropy of OPA during deformation and how it is affected by the presence of water. This, combined with AE monitoring, may help to better characterize the deformation mechanisms and microstructural changes during the deformation of OPA and how they are influenced by the stress orientation relative to pre-existing structural fabrics and the presence of water. In the end, this understanding may aid in the development of constitutive models that may be used to predict the anisotropic rheological behavior and long-term integrity of the material.

2 Experimental Materials and Methods

2.1 Material Characterization and Sample Preparation

The sandy facies of OPA is one of the three sub-facies types that were identified at the MT URL (Thury and Bossart 1999; Pearson et al. 2003). In comparison to the more prominent shaly facies of OPA, the fabric of the sandy facies (Fig. S1) is heterogeneous and characterized by alternating dark-grey, clay mineral-dominated layers and light gray lenses and layers of silt to sand-sized quartz and feldspar grains (Lauper et al. 2018, 2021; Kneuker and Furche 2021). The sandy facies generally contains more quartz and feldspar and less clay than the shaly facies (Pearson et al. 2003; Schuster et al. 2023). Sand layers are characterized by a grain-supported framework of quartz, carbonates and feldspars with a barely compacted clay matrix, which is filling the interparticle space (Fig. S2a). Clay layers are dominated by the clay-rich matrix with mineral grains showing a smaller grain size compared to sand layers (Fig. S2b).

The sample material investigated in this study was provided by Swisstopo (Federal Office for Topography, Wabern, Switzerland) and originates from two drill cores (BFI-1 and BFI-2) from the MT URL. Drilling of 101 mm diameter cores was performed perpendicular (BFI-2) and parallel (BFI-1) to the local bedding orientation within the sandy facies at dry conditions using compressed air flushing. Tested samples belong to core sections drilled 8–8.35 m (BFI-1) and 4–4.4 m (BFI-2) into the gallery wall. They were stored in plastic liners after extraction and vacuum-sealed in aluminum foil.

For triaxial testing, two cylindrical samples with a diameter of 50 mm were drilled parallel (p-sample) and perpendicular (s-sample) to the bedding orientation (Fig. S1), respectively, at dry conditions and then precision ground to a final length of 100 mm. After preparation, one set of "dry" p- and s-samples was carefully dried at 50 °C at a relative humidity (RH) of about $22 \pm 5\%$ until constant weight was reached, revealing a residual water content of ≈0.4 wt% compared to several sub-samples that were dried at 110 °C for > 48 h. A second set of "wet" p- and s-samples was stored in a desiccator at room temperature exposed to a relative humidity of $95 \pm 5\%$ that was achieved by employing a vapor equilibrium technique using a supersaturated K_2SO_4-solution (e.g., Laloui et al. 2013). Bulk density of the tested samples was determined from the ratio of weight to volume, revealing a density of 2.36 ± 0.01 g/cm^3 on average for dried and 2.51 ± 0.03 g/cm^3 for saturated samples. The average sample porosity is 12.6 ± 0.4 vol%, determined from a He-pycnometer-derived (Micromeritics, AccuPyc 1340) average grain density of 2.70 ± 0.02 g/cm^3 for sandy facies samples from the same drill core (BFI-1) (Schuster et al. 2021). Accordingly, the "wet" samples showed a degree of saturation > 95% after the saturation procedure, whereas the residual saturation of "dry" samples was estimated to be ≈8%.

All samples were equipped with four pairs of biaxially stacked rosette strain gauges (120 Ω Tokyo Sokki TML-FCB), each measuring vertical and radial strain, which were glued on the sample surface (Fig. S3) before inserting the samples into a neoprene jacket of 2 mm thickness to prevent intrusion of the confining medium (oil). The jacket was perforated with holes of 1 cm diameter allowing to glue 14 piezoelectric P-wave transducers (1 MHz resonant frequency) encapsulated into brass housings on the sample surface. This set of transducers enables recording of acoustic emissions (AE) and ultrasonic P-wave velocities during

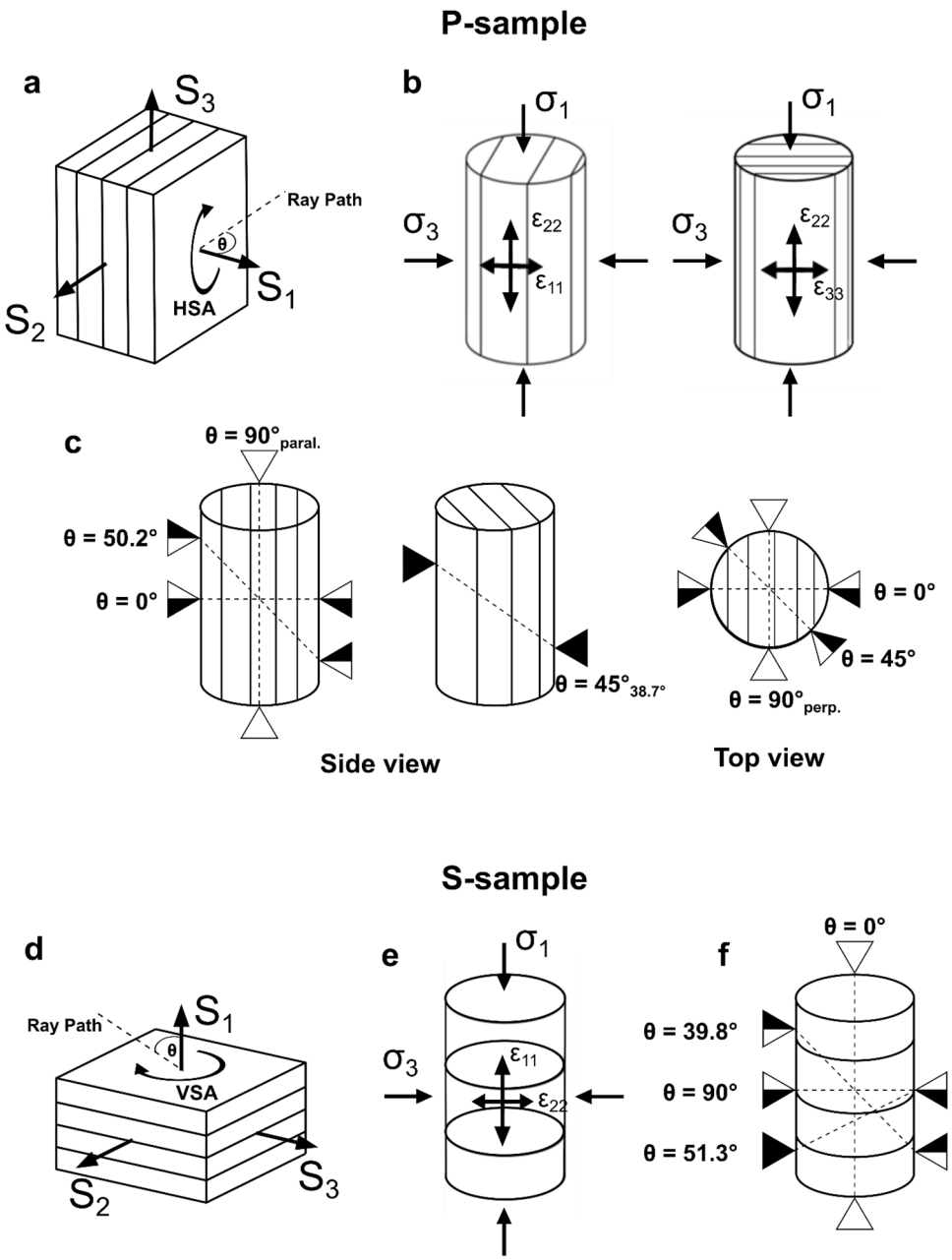

Fig. 1 Schematic showing the definition of coordinate system (**a**, **d**), strain (**b**, **e**) as well as the convention of ray path angle (**c**, **f**) for the case of transverse isotropy used in this study. θ defines the angle between the ray path and the horizontal (HSA) or vertical (VSA) symmetry axis for samples prepared parallel (p-sample) or perpendicular (s-sample) to bedding orientation. For p-samples, ray path angle rotates either axial (side view) or radial (top view) to the cylinder axis. Solid lines represent bedding planes, dashed lines in **c** and **f** represent ray path between P-wave transmitter and receiver

triaxial deformation (Fig. S3a). The positioning accuracy of the ultrasonic transducers (UT) on the sample surface was estimated to be about 1 mm. An additional pair of P-wave transducers was installed in the top and bottom steel plugs of the piston assembly, allowing to record P-wave velocity parallel to the sample axis. The applied sensor setup ensured the recording of elastic P-wave velocities along different ray paths oriented at an angle θ between the normal to the bedding plane (horizontal or vertical symmetry axis; c.f., Figs. 1a, d) and the ray path between UT sender and UT receiver.

2.2 Experimental Setup and Methods

Deformation experiments were performed at room temperature in a servo-hydraulic loading frame (Material Testing Systems, MTS; Stanchits et al. 2011) equipped with a triaxial cell using oil as confining medium. Hydrostatic pressure was increased to $p_c = 50$ MPa at a rate of 2 MPa/min and subsequently maintained constant for 18 h. Triaxial deformation tests at constant confining pressure were performed at unconsolidated undrained conditions using solid spacers at both sample ends. Therefore, the influence of pore pressure changes and effective stress on strength of saturated samples is not specified (c.f., Schuster et al. 2022). Axial loading was

applied at a constant displacement rate of 0.03 mm/min up to a total axial shortening (D_{tot}) of the specimens between 4.7 and 6.3 mm, measured externally by a linear-variable displacement transducer (LVDT) and corrected for system compliance. Total axial strain ($\varepsilon_{tot}=D_{tot}/L\times 100\%$) was determined from the initial sample length (L) and corrected axial displacement of the specimen (D_{tot}). True strain rate during triaxial deformation was estimated to be $\approx 4.8\times10^{-6}$ s^{-1}. Differential stress ($\sigma_{diff}=\sigma_1-p_c$) was measured with an accuracy of about ± 0.05 MPa by an internal load cell. Sample strain, recorded by four strain gauge pairs (Fig. S3a), follows the notation shown in Figs. 1b, e. Volumetric matrix strain was calculated by $\varepsilon_{vol}=\varepsilon_{ax}+2\times\varepsilon_{rad}$ from averaged axial and radial strain gauge readings. Deformation and mechanical data were recorded with a sampling rate of 2 Hz.

We calculated elastic parameters such as the Young's modulus (E) and Poisson's ratio (ν) from linear regressions on total axial strain (ε_{tot})—differential stress (σ_{diff}) and total axial strain (ε_{tot})—radial strain (ε_{rad}) curves (radial strain gauge readings), respectively. Due to the distinct non-linear strain hardening behavior (see chapter 3.1), linear regressions were applied in the interval between 0 and 0.5% total axial strain, regarded here as an "apparent" elastic modulus. We obtained the apparent Young's modulus E_1 from samples that were deformed perpendicular to bedding and E_2 from parallel oriented samples. Using the presented sensor setup (Fig. S3), we were able to determine three apparent Poisson's ratios, $\nu_{12}=-\varepsilon_{22}/\varepsilon_{11}$ from s-samples as well as $\nu_{23}=-\varepsilon_{33}/\varepsilon_{22}$ and $\nu_{21}=-\varepsilon_{11}/\varepsilon_{22}$ from p-samples (Fig. 1). Note that compressive stress and strain are denoted by a positive sign.

During loading, P-wave velocity measurements were performed from active ultrasonic transmission measurements every 15 s, using seven sensor pairs attached on the sample surface and one at the top and bottom of the sample. Each ultrasonic transducer pulsed with a 100 V amplitude for 3 µs with a time span of 5 ms between each sensor. Full waveform AE signals as well as ultrasonic velocity signals were amplified by 40 dB with a 100 kHz high-pass filter (Physical Acoustic Corporation) and recorded at a sampling rate of 10 MHz with an amplitude resolution of 16 bit using a 16-channel transient recording system (DAXBox, Prökel). P-wave arrival times along selected ray paths (crossing the sample's symmetry axis) were picked using the Akaike information criterion (AIC) and P-wave velocities were calculated from the distance between each sensor pair corrected for sample deformation determined from strain measurements. Note that changes in diameter were assumed to be homogeneous in the sample, neglecting inhomogeneous sample barreling during differential loading. For p-samples, five velocity traces were measured. Three traces (Fig. 1c) were measured either horizontally around the sample (in a plane perpendicular to the loading direction) at angles of $\theta=90°_{perp.}$, 45° and 0° (Fig. 1c top view) or at angles of $\theta=90°_{paral.}$, 50.2° and 0° (Fig. 1c side view) relative to the normal of the bedding and sample axis (propagation of wave is parallel to bedding and sample axis). Another trace ($\theta=45°_{38.7°}$ in Fig. 1c side view) was measured at $\theta=45°$ at an angle of $\beta=38.7°$ relative to the normal of the sample axis (sensor pair I5/R13 and C11/W7 c.f., Fig. S3a). For s-samples we estimated P-wave velocities at four different angles with respect to bedding at angles of $\theta=90°$, 51.3°, 39.8° and 0° (Fig. 1f). Redundant wave traces from similar angles were averaged. The absolute error of the P-wave velocity was estimated to be $\leq 5\%$, resulting mainly from the uncertainty in the determination of the propagation distance between the ultrasonic sensors (≈1 mm) and in travel time picking (≈0.1 µs). Noise from all determined velocities was reduced by applying a 10th-order median filter. In this study, we explicitly report on group (ray) velocities, which are equal to phase velocities in transverse isotropic media when the wave propagation direction coincides with the symmetry axis, thus at $\theta=0°$ and 90° (e.g., Dellinger and Vernik 1994; Johnston and Christensen 1995; Hornby 1998). Due to the size of the P-wave transducers (1 cm diameter) relative to the wave propagation distance, the remaining, off-axis velocity measurements are expected to be group velocities (Dellinger and Vernik 1994; Dewhurst and Siggins 2006). The difference between phase and group velocity is expected to be less than the estimated 5% uncertainty for P-wave velocity measurements, so the measured group velocities and ray angles can be assumed to be reasonable approximation for phase velocity and angle, respectively (c.f., Sarout et al. 2014a, b).

2.3 Microstructural Imaging

Structural analysis of deformed samples was performed using a micro X-ray computer tomography system (GE Phoenix X-ray Nanotom 180 NF) operated at 140 kV and 100 µA with a 5-megapixel digital detector and a voxel size resolution of 30 µm. Furthermore, microstructural imaging was done using a scanning electron microscope (FEI Quanta 3D Dual Beam). To this end, rectangular sub-samples ($11\times8\times3$ mm^3) were cut from the undeformed material and tested specimens followed by pre-polishing with SiC grinding paper down to P4000 grit for subsequent BIB polishing (JEOL IB-19520CCP). A layer of approximately 100 µm thickness was removed on an area of ≈2.5 mm^2 after a polishing time of 2 h at 8 kV, 200 µA and 6 h at 6 kV, 150 µA. BIB cross sections of tested specimens were prepared parallel to loading direction. Microstructural observation on carbon-coated BIB cross sections was performed at 20 kV acceleration voltage and 5 mm working distance.

Semiquantitative geochemical analysis was conducted with an attached EDAX energy-dispersive X-ray analyzer (EDX).

3 Results

3.1 Mechanical Deformation Behavior

Stress–strain curves of the tested samples reveal semi-brittle flow and ductile deformation characteristics at the applied conditions with distinct non-linear strain hardening behavior before failure. Deformation and mechanical behavior are strongly affected by loading orientation with respect to bedding as well as by the saturation state (see also Table 1. of the supporting material).

The p-sample deformed at dry conditions (Fig. 2a) reaches a peak stress of σ_{max} ≈152 MPa at a total axial strain of ≈3.2%. At peak stress, failure occurred with a stress drop of ≈-25 MPa, beyond which an almost constant residual stress is maintained. In comparison, the stress–strain curve of the dried s-sample (Fig. 2c) is characterized by ductile behavior with a peak differential stress of about 148 MPa at a total axial strain of about 3.5%, followed by minor post-peak weakening (< -6 MPa). Elastic anisotropy between p- and s-sample orientation was found to be higher (E_2 / E_1 = 13.9 GPa / 8.9 GPa ≈ 1.56) compared to strength anisotropy ($\sigma_{max\,2}$ / $\sigma_{max\,1}$ = 152 MPa / 148 MPa ≈ 1.03).

Wet samples (Figs. 2b, d) deform more ductile compared to dry samples. The p-sample shows only slight weakening (− 5 MPa), while the s-sample shows no weakening at all. In addition, peak strength and Young's modulus are strongly reduced due to the increased water content by about 34% ($\sigma_{max\,2}$ = 99 MPa) and 33% (E_2 = 9.3 GPa) in p-orientation and 46% ($\sigma_{max\,1}$ = 80 MPa) and 31% (E_1 = 6.1 GPa) in s-orientation, respectively. Elastic anisotropy remains relatively constant (E_2 / E_1 ≈ 1.51), whereas strength anisotropy increased ($\sigma_{max\,2}$ / $\sigma_{max\,1}$ ≈ 1.24) compared to dry conditions.

Averaged local axial strain is greatest in s-samples and increases at almost the same rate as total axial strain before peak stress is reached, suggesting homogeneous deformation (Fig. 2c, d). In contrast, averaged local axial strain of p-samples increases at a significantly reduced rate after reaching peak strength (Fig. 2a, b). In addition, axial strain ε_{22} is higher measured perpendicular (orange line Fig. 2a, b) to the bedding plane than parallel to it (blue line Fig. 2a, b), whereby local strains increasingly diverge with increasing total axial deformation. These trends were also observed for averaged radial deformation, showing larger expansion across than within the bedding layer as well as a distinct change of radial strain gradient after peak strength (Fig. 2a, b). Both observations indicate opening of bedding planes in p-samples and strain localization, which is more pronounced for the dried sample than for the wet sample.

Similar to axial strain, s-samples show larger averaged radial strain also after reaching peak stress (Fig. 2c, d). Determination of the apparent Poisson's ratio from total axial and averaged local radial strain during quasi elastic deformation yields similar values for dried p- (0.09–0.13) and s-samples (0.11). The apparent Poisson's ratio increases significantly for wet samples (Fig. 2b, d), with the s-orientation showing an increase by a factor of >2 (0.28).

Elastic wave velocity evolution, cumulative AE as well as averaged volumetric strain and differential stress are shown in Fig. 3 as a function of total axial strain. Local averaged volumetric strain of the dry p-sample (grey line in Fig. 3a) shows the transition from compaction to dilation (after maximum compaction) at total axial strain of ≈1.7%. Maximum dilation occurs before stress drop. Absolute volumetric compaction of the dried s-sample is larger (≈1.1%) than for the p-sample (≈0.75%, grey lines in Figs. 3a, c). The transition from compaction to dilation occurs at a total axial strain of ≈2.4%, whereas the s-sample dilates mostly during post-peak strain weakening. For the wet p-sample, dilation is strongly suppressed and the transition from compaction to dilation shifts to larger total axial strain (3%) close to the peak strength (grey line in Fig. 3b). The saturated s-sample displays significantly reduced compaction compared to the dry sample (≈− 70%), but strongly increased dilation (Fig. 3d). Similar to the dried s-sample, the transition to dilation is reached before peak strength.

3.2 Ultrasonic Velocities and Acoustic Emission Activity

Similar to mechanical data, recorded P-wave velocities as well as AE are strongly influenced by sample orientation and water saturation. At hydrostatic conditions, all samples show that the sandy facies can be described as a transversely isotropic material (hexagonal symmetry; c.f., Fig. 1a, d), as commonly assumed for OPA and other clay-rich sedimentary rocks and shales (e.g., Thomsen 1986; Johnston and Christensen 1995; Vernik and Liu 1997; Wang 2002; Sarout et al. 2007; Sarout and Guéguen 2008; Sayers 2013; Sarout et al. 2014a, b; Bonnelye et al. 2017; Lozovyi and Bauer 2019; Yurikov et al. 2019).

The initial P-wave velocities (V_p^0) of the dried samples at a confining pressure of 50 MPa range between ≈3.0 and 3.8 km/s (Fig. 3), whereby P-wave velocity is highest parallel to bedding (θ = 90°) and lowest perpendicular to it (θ = 0°). Comparing p- and s-samples, p-wave velocities measured at the same angle θ show only moderate conformity, which may be explained by the compositional heterogeneity of the sandy facies of OPA.

The elastic wave velocities of the dried p-sample (Fig. 3a) may be divided into two groups: velocities that were measured in a horizontal plane at different azimuths (θ = 0°, 45°

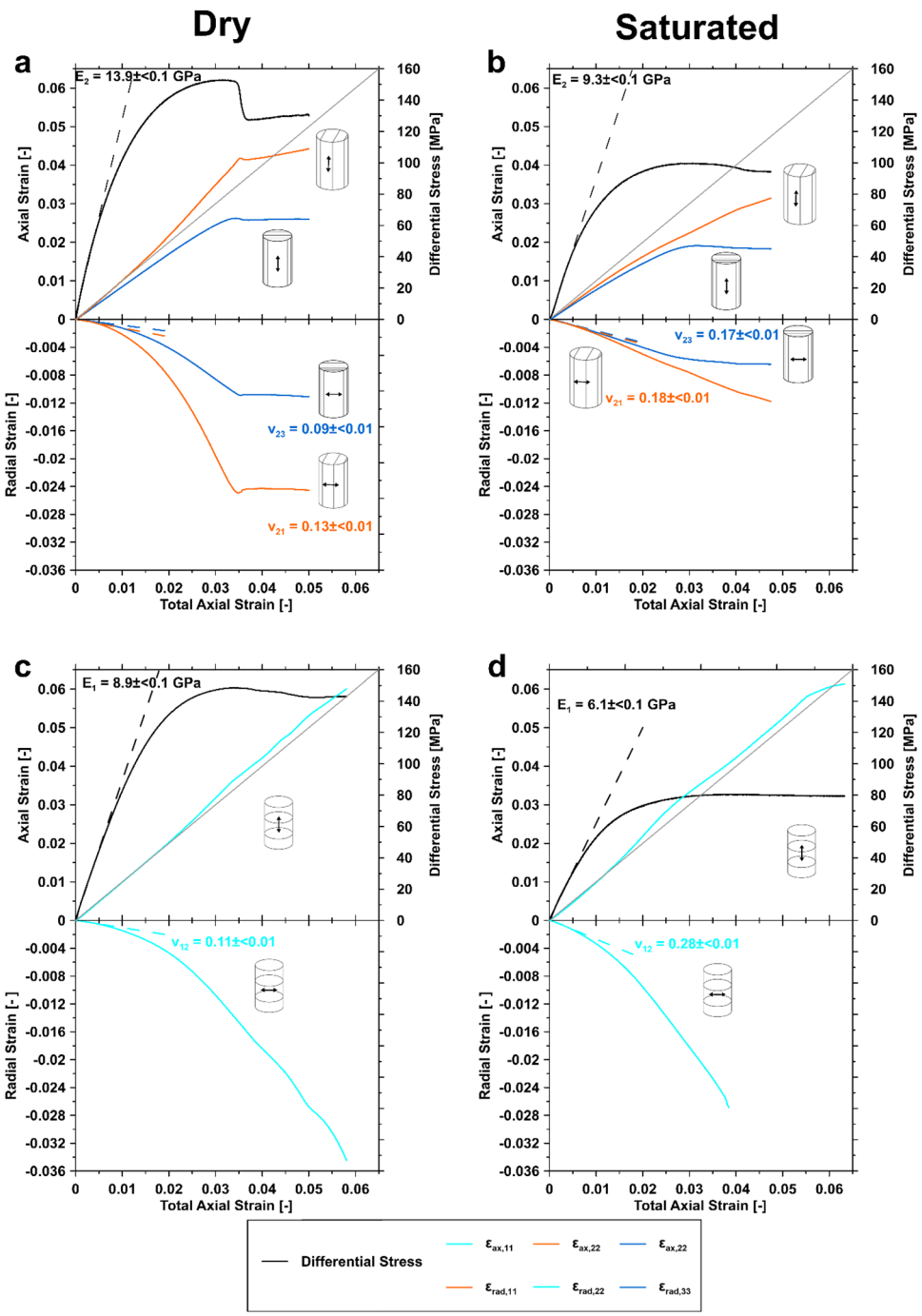

Fig. 2 Stress-total strain curves of the sandy facies of OPA deformed parallel (**a**, **b**, p-samples) and perpendicular (**c**, **d**, s-samples) to bedding at a confining pressure of 50 MPa. Local averaged axial (ε_{ax}) and radial (ε_{rad}) strain (c.f., Fig. 1 for nomenclature) are plotted against total axial strain, showing the influence of water saturation on deformation behavior. The apparent Young's modulus was determined from linear regressions during quasi elastic deformation (black dashed line) from differential stress and total axial strain, while the apparent Poisson's ratio was determined from linear regressions (dashed lines) from averaged local radial strain and total axial strain. Local axial and radial strain of p-samples (**a**, **b**) were measured within (blue line) and parallel to the bedding plane (orange line). Note the failure of two radial strain gauges of the saturated s-sample before the experiment was terminated (**d**). The gray line shows a gradient of one of total strain versus local axial strain

and 90°$_{perp.}$) and in a vertical plane rotating axially (polar direction) around the stress axis ($\theta = 50.2°$ and 90°$_{paral.}$), showing a different evolution during deformation. For the horizontal group, P-wave velocities increase only slightly ($\approx < 0.04$ km/s) with increasing deformation up to a total strain of ≈1% where a velocity maximum is reached. Beyond ≈1% strain, P-wave velocities decrease significantly (− 0.25 to − 0.46 km/s) until the end of deformation. For the second velocity group ($\theta = 50.2°$ and 90°$_{paral.}$), P-wave velocities also increase initially and reach a maximum followed by velocity reduction. However, the total strain at which the velocity maximum is reached increases with increasing θ ($\varepsilon_{tot} \approx 1\%$ for $\theta = 50.2°$, $\varepsilon_{tot} \approx 1.5\%$ for $\theta = 0°$ and $\varepsilon_{tot} \approx 2.2\%$ for $\theta = 90°$ $_{paral.}$). The onset of AEs coincides with onset of dilation, indicated by a non-linear increase of volumetric strain and P-wave velocities, as microcracks form. After the onset of volumetric dilation, AE rate increases non-linearly and reaches a maximum rate during the stress drop, observed at $\varepsilon_{tot} \approx 3.5\%$.

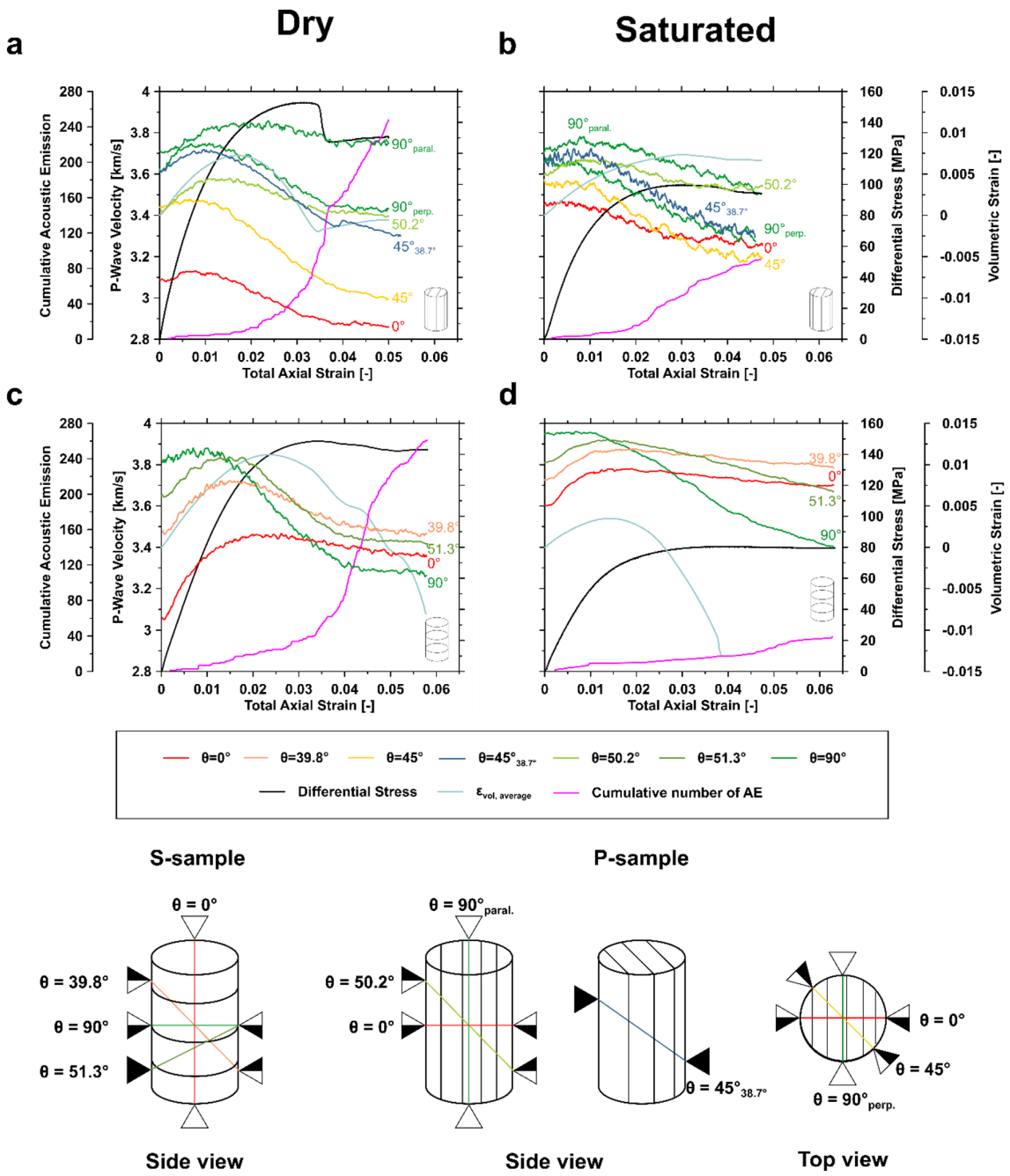

Fig. 3 Differential stress, averaged local volumetric strain (ε_{vol}), cumulative acoustic emission (AE) and P-wave velocities as a function of total axial strain for dry and saturated samples in p- (**a**, **b**) and s-orientation (**c**, **d**), deformed at 50 MPa confining pressure. The color scale of P-wave velocities indicates the inclination of the ray path propagation relative to bedding from low (green) to large (red) angles. For p-samples, elastic wave velocities at an angle of $\theta = 0°$, 45° and $90°_{perp.}$ were measured perpendicular to the cylinder axis and $\theta = 0°$, 50.2° and $90°_{paral.}$ in a vertical plane along the stress axis (see schematic below). Note the reduced volumetric strain data for the saturated s-sample (**d**) due to strain gauge failure

P-wave velocity evolution during deformation is considerably different for the dry s-sample (Fig. 3c). The initial increase of P-wave velocities with axial strain becomes more pronounced with decreasing θ angles and is larger in comparison to similar ray paths in the dried p-sample. Hence, P-wave velocities increase with the propagation direction relative to bedding from $\theta = 90°$ ($\approx +0.06$ km/s) to $\theta = 0°$ ($\approx +0.41$ km/s). The onset of dilatancy is indicated by increasing AE activity and a decreasing volumetric compaction rate. P-wave velocity measured

perpendicular to bedding ($\theta = 90°$) reaches a maximum at ≈ 1% total axial deformation followed by a continuous decrease until the end of deformation. The remaining ray paths also show a P-wave velocity maximum followed by decreasing velocities. The total axial strain at the velocity maximum increases with decreasing θ (with largest strain at velocity maximum for $\theta = 0°$). The absolute P-wave velocity reduction is highest for $\theta = 90°$ (≈− 0.6 km/s), leading to a reversal of the initial P-wave anisotropy. Bedding parallel P-wave velocity as shown in Fig. 3c was averaged from 5 different sensor pairs (G1/V3, O2/B4, I5/W7, A8/P6, H9/U10 and C11/R13, c.f., Fig. S3a), all showing an almost identical velocity evolution during deformation with a maximum standard deviation of 50 m/s. Cumulative number of AE increases almost linearly with deformation at a relative constant rate up to a total axial strain of ≈3.3% and increases significantly after the peak stress.

For wet samples (Fig. 3b, d), initial P-wave velocities (V_p^0) increase for both orientations, ranging between ≈3.45–3.95 km/s. However, the increase is higher at low θ angles, which results in a reduction of the initial velocity anisotropy of saturated samples ($V_{p,\theta=90°}/V_{p,\theta=0°} = 1.07–1.10$) in comparison to dried samples ($V_{p,\theta=90°}/V_{p,\theta=0°} = 1.20–1.25$). During loading, wet samples also show an initial increase of P-wave velocities along the different ray paths. Again, the largest absolute velocity increase is found for $\theta = 90°_{\text{paral.}}$ in p-samples and for $\theta = 0°$ in s-samples. However, the absolute increase is much lower (≈1.5–4.8%) compared to dry samples (1.1–13.1%). In addition, the total number of recorded micro acoustic events reduces drastically at high saturation.

For the saturated p-sample (Fig. 3b), P-wave velocity evolution during deformation can also be divided into two groups, with relatively similar trends compared to the dry sample. However, the absolute velocity reduction along $\theta = 90°_{\text{perp.}}$ is greater (≈-0.38 km/s) for the wet sample, whereas the reduction along the other ray paths is lower compared to the dry sample, which agrees with observed higher volumetric compaction. Due to the larger increase of P-wave velocity measured at $\theta = 0°$ in comparison to the other direction, we observe a reduction and even a reversal of the initial anisotropy of the velocities measured in azimuthal direction ($\theta = 0°$, 45° and $90°_{\text{perp.}}$), which was not observed in the dry sample.

Although dilation and thus the opening of microcracks perpendicular to bedding ($\varepsilon_{rad,21}$) is more pronounced than parallel to bedding ($\varepsilon_{rad,23}$) for both p-samples (c.f., Fig. 2a, b), the relative velocity reduction along $\theta = 0°$ is comparable to $\theta = 90°_{\text{perp.}}$ (Fig. 3a, b). The latter observation suggests that vertical microcracking is not exclusively parallel to the bedding. Consequently, the elastic symmetry of p-samples is altered during differential loading, so that the initial assumption of a transversely isotropic medium is no longer valid for this sample orientation.

The P-wave evolutions for saturated s-sample (Fig. 3d) and dry sample are comparable, also showing a velocity anisotropy reversal. As observed in the saturated p-sample, P-wave maxima for the different ray paths are also reached at lower total axial strains (< + 1.5%) than for the dry sample.

3.3 Deformation Structures

Deformed dry samples in p- and s-orientation (Figs. 4a, c) show a major shear fracture along which the samples disintegrated after removal from the jacket. A CT-scan of the p-sample (Fig. 4a) shows a major shear plane crossing the whole sample complemented by several sub-parallel shear fractures distributed within the sample. Shear zones are discrete with an average width of ≈1 mm and oriented oblique to the bedding planes at an inclination of ≈30° to the cylinder axis. The s-sample (Fig. 4c) also displays one major shear zone (width ≈1 mm), inclined at about 40° to the loading direction, crossing the entire sample. In addition, some smaller shear fractures developed sub-parallel to the major shear zone. In contrast to the p-sample, multiple horizontal fractures developed parallel to the bedding plane orientation, which are presumably artifacts created during unloading. Furthermore, the sample exhibits slight bulging, suggesting that the strain is more distributed compared to the p-orientation.

No discrete, continuous shear fracture plane developed in the saturated samples of both orientations. Instead, both samples display slight (p-sample) to pronounced (s-sample) barreling. The wet p-sample (Fig. 4b) shows the development of conjugate shear fractures close to the sample surface. In addition, several discontinuous shear fractures inclined ≈40° to the sample axis are present in the sample interior. The saturated s-sample (Fig. 4d) shows the highest degree of barreling with well-developed conjugate shear fractures.

BIB-cross sections of deformed samples were prepared outside (Fig. 5) as well as inside (Fig. 6) of the macroscopically visible shear zones in different compositional layers (grain or matrix supported). Deformation microstructures reveal heterogeneous strain accumulation by a combination of brittle cataclasis and frictional granular flow (grain rotation, microcracking, frictional sliding) as well as intracrystalline plasticity of phyllosilicates (bending and kinking). The contribution of each deformation mechanism is determined by composition, water content, and sample orientation.

P-samples show a high density of inter- and transgranular microcracks, oriented parallel to bedding plane orientation and several micrometers wide (Fig. 5a, c—arrow 1), suggesting facilitated crack propagation due to the parallel orientation of bedding and loading axis. Stress concentration at grain contacts of single non-phyllosilicate

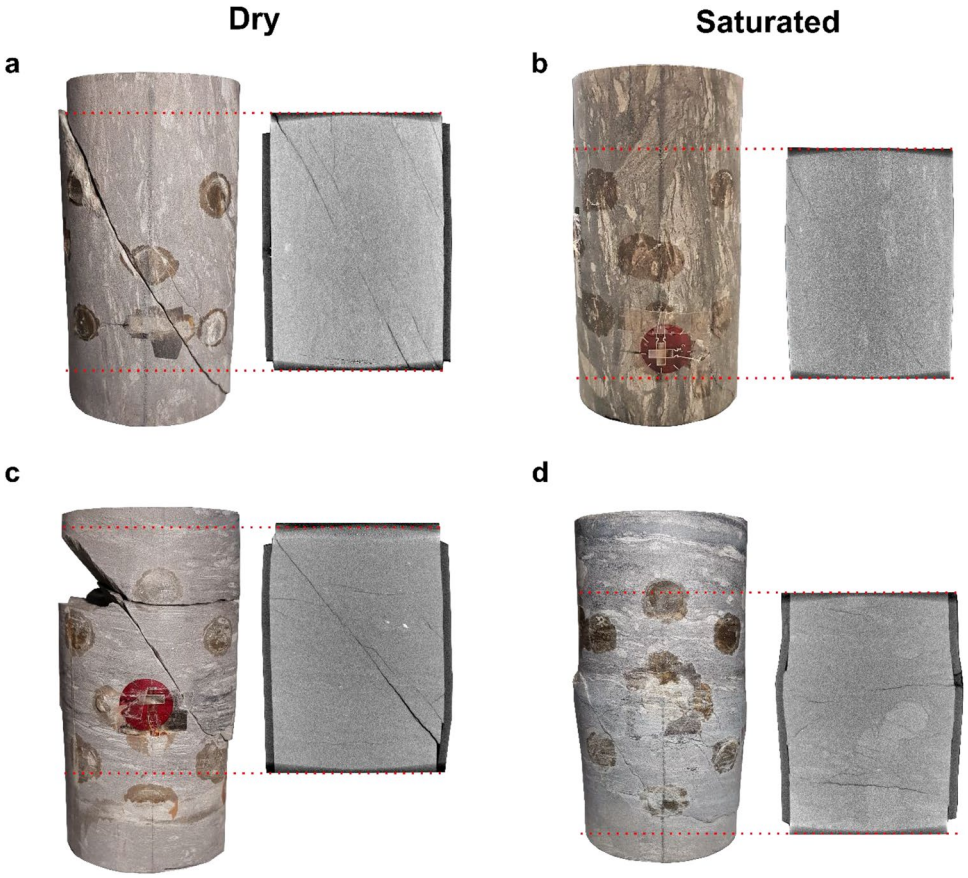

Fig. 4 Post-deformation images and CT-scans of dry and saturated samples tested parallel (**a**, **b**) and perpendicular (**c**, **d**) to bedding orientation. Note that CT scans show central sections of the entire sample due to the limited imaging area of the used µCT system (approximate imaging area is indicated by the red dotted lines). Initial sample length and diameter of the tested samples are 100 mm and 50 mm, respectively

minerals is demonstrated by intragranular impingement cracks. Microcracking of phyllosilicates in the compacted matrix is intergranular (Fig. 5a—arrow 2). Fracture density decreases significantly in highly cemented sand layers (Fig. 5c). The clay mineral matrix between grain-supported mineral clasts shows an almost intact pore structure (Fig. 5c—arrow 2), indicating limited compaction in contrast to matrix-supported domains (Fig. 5e). Here, compaction is accommodated by pore collapse and alignment of clay minerals parallel to bedding and around larger mineral clasts (Fig. 5e—arrow 1). Axial deformation is illustrated by stretched framboidal pyrite as well as bent and kinked micas (Fig. 5a—arrow 3 and Fig. 5e—arrow 2).

In s-samples we observe matrix compaction (Figs. 5b, f) by interparticle sliding, bending and kinking and pore collapse (Fig. 5b—arrow 3). Clay minerals are aligned with their longest axis perpendicular to the loading direction and parallel to bedding. Quartz, feldspar and calcite show few intragranular microcracks, which opened sub-perpendicular to the σ_1-direction at grains that are in contact with each other (Fig. 5b, d). However, microcrack connectivity is limited in this direction as cracks in isolated grains appear to be blunted by the surrounding clay matrix (Fig. 5b—arrow 1). Stretched micas become locally fractured and boudinaged (Fig. 5b—arrow 2, Fig. 5f—arrow 1), indicating horizontal extension. Similar to p-samples, compaction of clay matrix is limited in grain-supported layers (Fig. 5d—arrow 2).

The deformation microstructures are qualitatively similar for dry and saturated samples, suggesting similar deformation mechanisms. However, microcrack density is lower in saturated compared to dried samples indicated optically and in agreement with the reduced number of total acoustic emission and smaller P-wave velocity reduction (especially for the saturated s-sample). We observe several undulating, µm-thick shear bands that develop sub-parallel to bedding as alignment of clay minerals and neighboring particles primarily in matrix-supported layers (Figs. 5e, f). The layers are bent, rotated and delaminated according to the local shear direction (Fig. 5e—arrow 1, Fig. 5f—arrow 2). In p-direction, shear bands often develop around grain boundaries of stronger mineral clasts, whereas localized clay particle alignment in conjugate shear bands results in the development of elongated lensoid microlithons in s-direction, indicatiing bulk flattening (c.f., schematic sketch in Fig. 5f).

Our observations suggest that compaction of pore space as well as interparticle sliding and bending of clay minerals are the dominant deformation mechanisms in the clay-rich layers, whereas microcracking predominates in sand-rich layers.

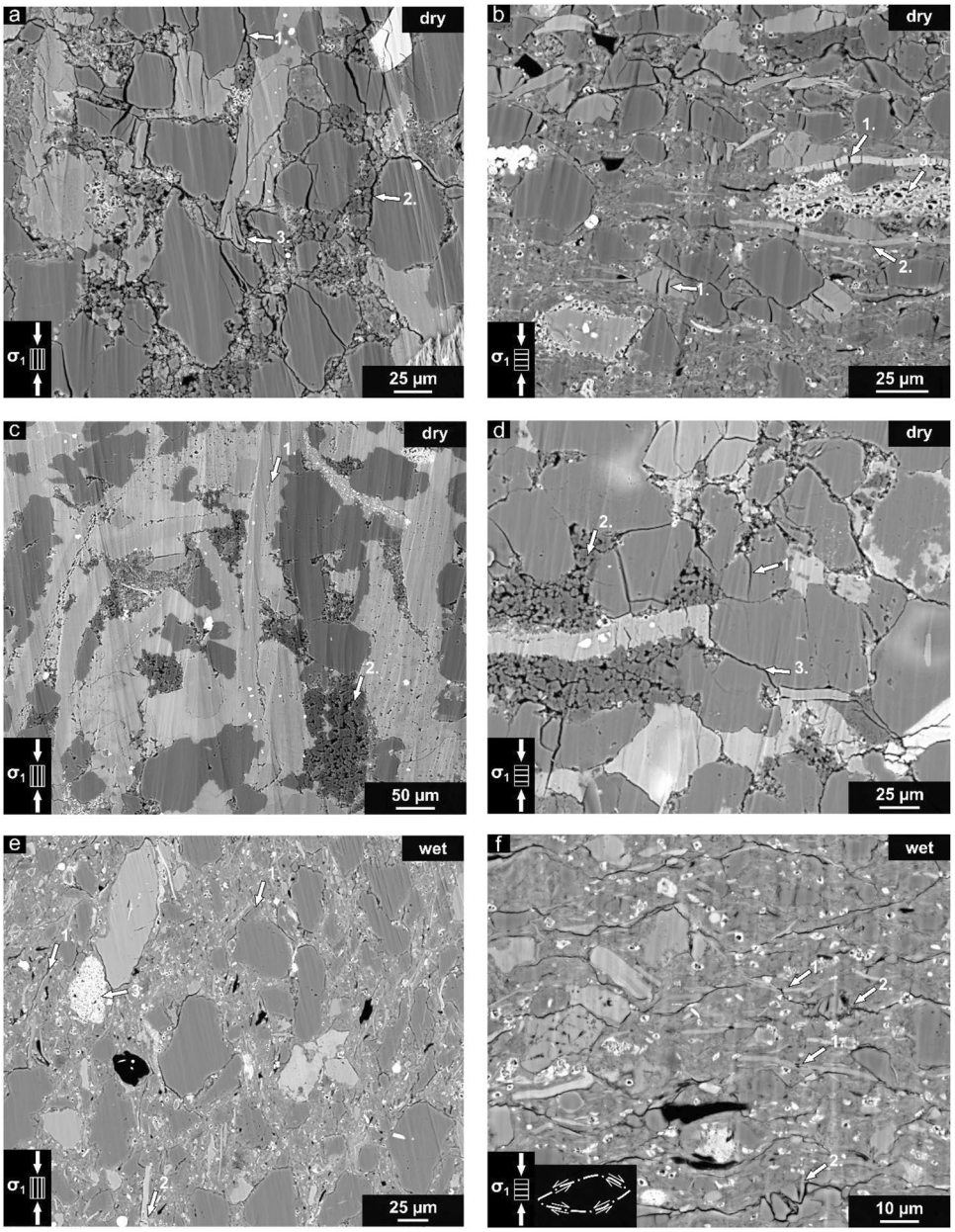

Fig. 5 Backscattered electron microscope images of deformation structures outside of developed shear zones in dry (**a**—**d**) and wet (**e**, **f**) samples. Loading direction with respect to bedding orientation is indicated in the black boxes at the bottom left of each image. The schematic sketch at the bottom left of image **f** indicates the local shear direction of undulating shear bands that form microlithons in clay layers of the wet s-sample. Details labeled by numbers are described in the text (c.f., Chapter 3.3)

Shear zones (Fig. 6) are characterized by microstructures indicative of enhanced shear localization. Localization and shearing are accommodated by bending and rotation of mineral grains modifying the initial fabric orientation. In addition, enhanced microcracking and grain size reduction by comminution of non-phyllosilicate minerals resulted in an increased porosity. Shear zone boundaries (dotted lines in Fig. 6), especially in s-samples, show a transitional increase in shear strain intensity towards the center. This is highlighted by the asymmetric opening of cracked rigid minerals (Fig. 6b—arrow 2, 6c—arrow 2, 6f—arrow 3) as well as stretching, bending and delamination of phyllosilicates (arrow 1 in Fig. 6b, d, e, f). Deformation and formation of ductile shear zones produced a sigmoidal foliation by progressive rotation of minerals subparallel to the shear plane. Fabric rotation towards the shear zone is up to 135° in p-samples. For s-samples fabric rotation is only 40° with wider shear zones than p-samples. Furthermore, shear zones are wider in the presence of water. Strain inside the shear zones is heterogeneously distributed and accommodated by a combination of cataclastic flow, including comminution and rotation of quartz, feldspar and calcite (Fig. 6a—arrow 1, 6b—arrow 3, 6c—arrow 1), as well as frictional granular sliding, bending and kinking of phyllosilicates (Fig. 6d—arrow 2, 6e—arrow 2). The internal fabric of the shear zones is characterized by an S-C foliation (e.g., Berthé et al. 1979; Rutter et al. 1986; Volpe et al. 2022; see dash-dotted lines

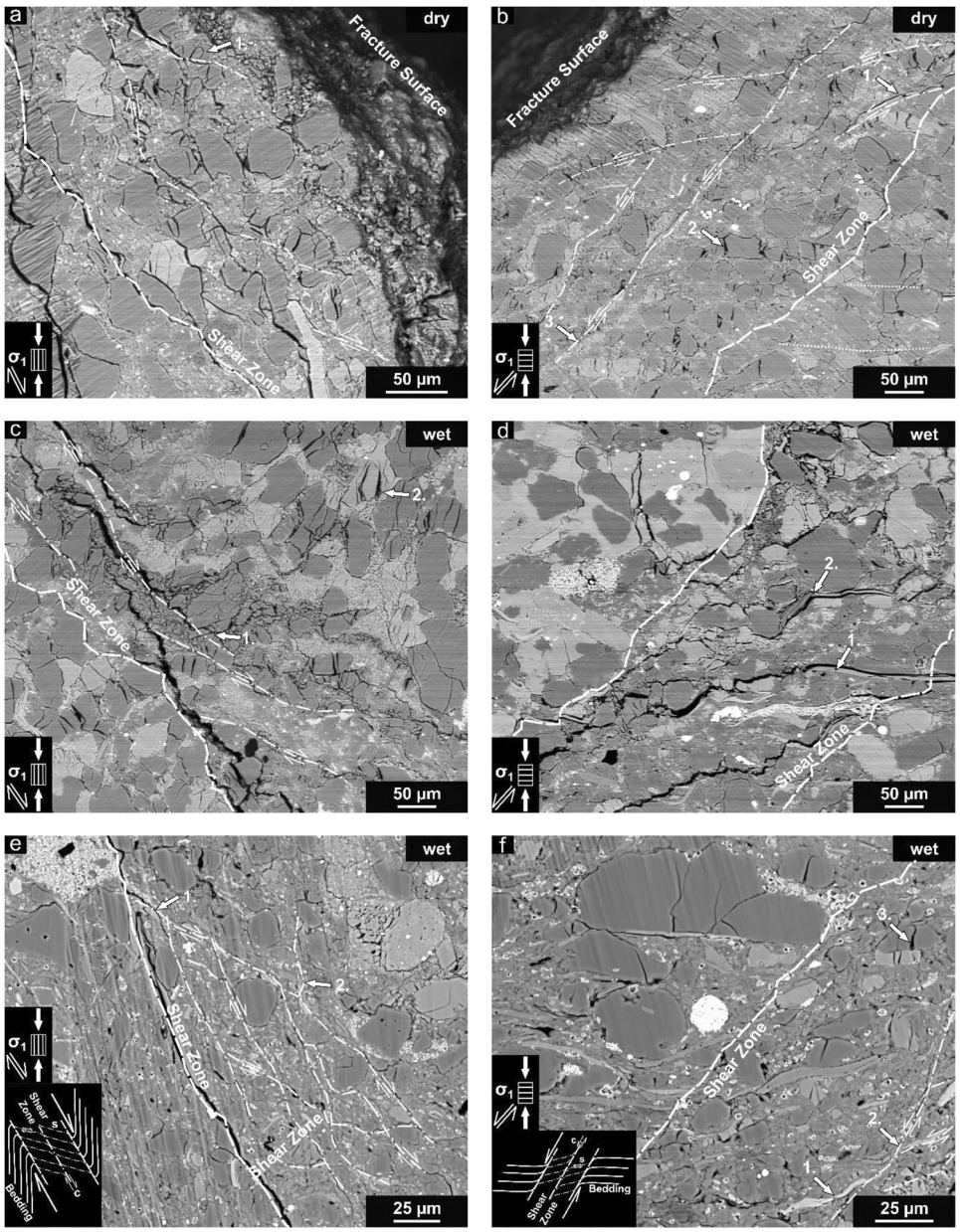

Fig. 6 Backscattered electron microscope images of developed shear zones in dry (**a**, **b**) and wet (**c**—**f**) samples. Loading direction with respect to bedding orientation is indicated in the black boxes at the bottom left of each image. Shear zone boundaries are indicated by dashed lines. Dash-dotted lines represent internal shear bands, which form an S-C-like fabric (shown in the bottom left of **e** and **f**) within the shear zone. Further details, also labeled by numbers, are described in the text (c.f., Chapter 3.3)

in Fig. 6 with local shear direction indicated by arrows and schematic insets shown in Figs. 6e, f) along which trails of comminuted rigid grains (arrow 1 in Fig. 6c) and phyllosilicates (parallel to their longest axis) are aligned (Fig. 6b—arrow 1, 6b—arrow 3, 6e—arrow 2, 6f—arrow 2). The contribution of cataclastic flow decreases in matrix-supported layers, especially in water saturated samples, in which rigid grains seldomly display microcracks (c.f., Fig. 6c–d), whereas foliation intensity increases. Although inspection of shear zone structures in dried samples was limited due to sample separation, disintegration along the shear zone suggests a higher degree of strain localization associated with more intense cataclastic grain comminution compared to saturated samples. In saturated samples, we find an increase of frictional sliding of phyllosilicates at the expense of microcracking of non-clay minerals and fracture propagation.

4 Discussion

The deformation behavior and mechanical properties (peak strength, Young's modulus and Poisson's ratio) of the sandy facies of Opalinus Clay are significantly affected by the orientation of bedding planes relative to

the maximum stress axis as well as the presence of water. In general, p-samples display a higher apparent Young's modulus in comparison to s-samples, independent of water content. Saturated samples display higher strength and elastic anisotropy, highlighted by significantly increased Poisson's ratio, as well as increased ductility, while the claystone samples become mechanically weaker and elastically more compliant. We observe a significant increase of initial P-wave velocities of saturated samples measured under hydrostatic conditions prior to axial deformation in both sample orientations, which is most pronounced for $\theta = 0°$. This results in reduced anisotropy compared to dry samples. Water saturation and sample orientation have a significant effect on P-wave velocities. This suggests that the elastic anisotropy of the sandy facies of OPA highly depends on the orientation of the microfabric (preferred orientation of minerals, pores, and microcracks) relative to the loading direction and magnitude.

In the following, we combine mechanical and acoustic data with observed deformation structures to discuss the influence of bedding orientation and water content on the observed deformation behavior and elastic anisotropy evolution of the sandy facies of OPA at the applied conditions. Finally, we compare our results to previous experiments and discuss factors that may control the stress-induced elastic anisotropy of shales.

4.1 Deformation Behavior and the Effect of Sample Orientation and Water

At the applied pressure conditions, sandy facies OPA exhibits a combination of distributed and localized brittle deformation such as microcracking, pore collapse, frictional particle sliding and bending and kinking of phyllosilicates, leading to a complex transitional behavior involving inelastic compaction and dilation. We observe that the orientation of the pre-existing microfabric and the presence of water play a significant role on fault propagation, failure stability and mechanical properties. Only the dry p-sample showed a marked stress drop, whereas the dry s-sample failed by stable, slow faulting. Water reduces strength and further enhances slow faulting, resulting in stable, increasingly delocalized failure. To characterize the underlying deformation processes, we combine mechanical and acoustic data and show the evolution of total mean stress $\sigma_{mean} = (\sigma_1 + 2 \times p_c)/3$ (neglecting pore pressure of wet samples) with volumetric strain (Fig. 7 a, b). In addition, we compile P-wave velocities measured perpendicular ($V_{\theta = 0°}$) and parallel to ($V_{\theta = 90°}$) to bedding plane orientation and determine the relative velocity change ($\delta V_p/V_p^0$) (Fig. 7 c, d) and P-wave anisotropy coefficient (A_p) in Fig. 7 e, f:

$$A_p = \frac{V^2_{\theta=90°} - V^2_{\theta=0°}}{2V^2_{\theta=0°}}$$

similar to Thomsen's anisotropy parameter ε (Thomsen 1986; Dewhurst et al. 2011). We regard this expression as a quantification of anisotropy without any reference to Thomsen's parameters, since the latter presuppose transverse isotropy (c.f., Dewhurst et al. 2011). We also determine A_p in the polar and azimuthal direction for deformed p-samples, using $V_{\theta = 90°paral.}$ and $V_{\theta = 90°perp.}$ (c.f., Fig. 3) as the bedding parallel velocity, respectively (Delle Piane et al. 2011).

The mechanical behavior of all samples differs (Fig. 7a, b), but in general their pre-failure behavior may be divided into three different stages: first, a short quasi elastic phase, followed by inelastic compaction up to a stress c_i at which dilatant microcracking is initiated, leading to cataclastic flow; second, a transient episode of simultaneous compaction and dilation and third, dilation at a critical stress c_d (Wong et al. 1992, 1997; Dresen and Evans 1993; Wong and Baud 2012).

The phase of inelastic volumetric compaction is characterized by an increase in P-wave velocities measured parallel to the σ_1-direction in both p- ($V_{\theta = 90°paral.}$) and s-sample ($V_{\theta = 0°}$) orientation (Fig. 7c, d), while velocities measured perpendicular to σ_1 remain almost constant. This presumably results from the closure of pore space, pre-existing fractures, and compaction-induced increase of total grain contact area and contact stiffening. Consequently, inelastic volumetric compaction leads to a decrease in anisotropy (A_p) of s-samples, but for p-samples to an anisotropy increase in polar direction, while the azimuthal anisotropy remains almost constant (Fig. 7e, f). The relative velocity increase and the contribution of compaction before reaching c_i is largest for dry samples and in s-orientation, which is due to the preferential orientation of compliant pores and microcracks perpendicular to the loading direction, resulting in greater strain accumulation and therefore in a lower Young's modulus compared to p-samples (Fig. 2). The lower velocity increase of saturated samples during volumetric compaction is due to the presence of water, which fills pores and pre-existing microcracks. This causes reduced compaction of saturated, bedding-parallel, low-aspect ratio pores and cracks in normal direction (e.g., Schoenberg and Helbig 1997; Sayers 2013) and enhances wave propagation speed, which results in higher initial P-wave velocity compared to dry samples (Fig. 3). Drying-induced dehydration leads to preferential opening and formation of compliant, desiccation-induced, bedding-parallel fractures (e.g., Peron et al. 2009; Wild et al. 2015), which results in decreasing initial P-wave velocity and increasing anisotropy (Fig. 7e, f). This relationship between P-wave velocity and water saturation has also been observed experimentally for several other shales

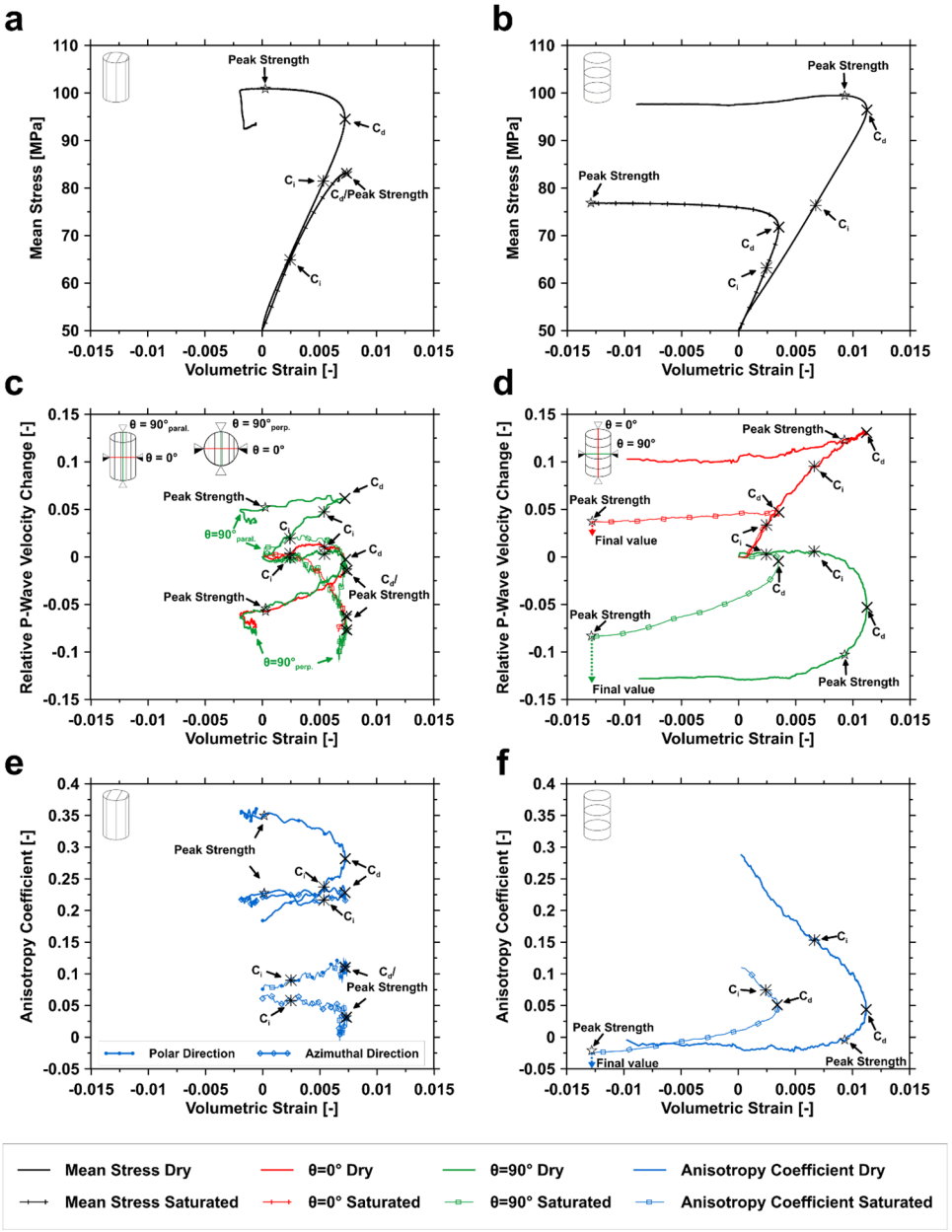

Fig. 7 Mean stress (**a**, **b**), relative P-wave velocity change (**c**, **d**), and anisotropy coefficient versus averaged local volumetric strain (ε_{vol}) curves for dry (continous line) and water saturated samples in p- (left column) and s-orientation (right column), deformed at 50 MPa confining pressure. The stress at the initiation of microcracking (c_i), the stress at the onset of dilation (c_d, reversal of volumetric strain) as well as the peak strength (star symbol) are shown for each experiment. θ denotes the angle of the P-wave ray path to the normal of the bedding plane (symmetry axis)

(e.g., Vernik and Liu 1997; Wang 2002; Valès et al 2004; Sarout and Guéguen 2008; Sarout et al. 2014a, b; Douma et al. 2019; Yurikov et al. 2019). However, the decrease of dynamic stiffness of pores and cracks due to dehydration is in contrast to the observed higher mechanical stiffness of dry samples. This may be explained by an increase in interparticle shear resistance of clay aggregates due to dehydration-induced capillary suction (Ferrari et al. 2014; Wild et al. 2015; Zhang 2017), leading to a shear stiffening of pores and microcracks (Sayers 2013). A similar mechanism was found experimentally by Yurikov et al. (2019) and Douma et al. (2019), who measured an increase in the dynamic horizontal shear modulus of the shaly facies of OPA and Whitby Mudstone with decreasing water saturation.

At the onset of cracking c_i, P-wave velocities measured perpendicular to the σ_1-direction in p- ($V_{\theta=0°}$, $V_{\theta=90°perp.}$) and s-sample ($V_{\theta=90°}$) orientation start decreasing (Fig. 7c, d). Microcracks form mostly parallel to the major stress axis and open perpendicular to it (e.g., Sayers and Kachanov 1995; Sayers 1999; Fortin et al. 2006; Stanchits et al. 2006). This behavior is accompanied by the onset of AE activity (Fig. 3). Beyond c_i, increasing propagation and opening of microcracks competes with simultaneous progressive compaction. Both processes are accompanied by an increase in P-wave velocity parallel to the loading axis, whereas P-wave velocities measured perpendicular to the loading axis decrease (Fig. 7c, d), further enhancing stress-induced anisotropy for p- and s-sample orientations

(Fig. 7e, f). This process is more pronounced at dry conditions, resulting from the higher initial anisotropy and the lower normal stiffness of pores and pre-existing cracks, showing a larger anisotropy reduction (s-orientation) or polar increase (p-orientation) in comparison to saturated samples (c.f., Sarout and Guéguen 2008; Douma et al. 2019). Azimuthal anisotropy of the saturated p-sample starts to decrease beyond c_i, but remains constant during the complete experiment for the dried sample. Approaching c_d, the σ_1-parallel P-wave velocity increase slows down, whereas for traces perpendicular to the sample axis, p-wave velocities reach a maximum at c_d. Total mean stresses at the onset of microcracking and dilation for dry samples are similar irrespective of sample orientation, while c_i and c_d of water saturated samples are significantly reduced (Fig. 7a, b).

We observe that the dry p-sample exhibits significantly greater volumetric dilation between c_d and peak stress compared to the s-samples. Shear enhanced dilation in p- sample orientation may also be related to the intense fabric rotation (up to 135°) observed in the vicinity of the developed shear zones (Fig. 6a, c, e; c.f., Winhausen et al. 2022). A gradual fabric rotation between c_d and peak stress is also indicated by the progressive reduction of $V_{\theta = 90° \, paral.}$ (Fig. 7c), suggesting asymmetric opening and rotation of microcracks (Fig. 6a, c). Shear fracture coalescence results in extreme strain localization (Fig. 2a) leading to failure within approximately 100 s.

The s-sample exhibits minor volumetric dilation between c_d and peak stress, followed by continued bulk deformation after failure, as indicated by local strain gauges (Fig. 2c). Dilatancy occurs mainly during slow, stable faulting between peak stress and residual stress over a period of about 3000 s. Microstructural examination of this sample also shows a transition zone close to the developed shear zone, characterized by local fabric rotation (~ 40°) with strain predominantly accommodated by granular flow and frictional particle sliding of phyllosilicates. This transitional zone is significantly wider compared to the p-sample, indicating shear zone thickening due to outward migration of strain gradients or shear zone margins. Both observations are associated with strain hardening and more stable failure behavior (e.g., Fossen and Cavalcante 2017).

Sandy facies Opalinus Clay became weaker in the presence of water. This may be caused by a combination of effects: first, as experiments were undrained, application of confining pressure likely produced excess pore pressure in saturated samples, reducing the initial effective mean stress before axial deformation. Pore pressure continues to increase during triaxial deformation due to volumetric compaction, further decreasing the effective mean stress (e.g., John et al. 1963; Ibanez and Kronenberg 1993; Islam and Skalle 2013; Wild and Amann 2018; Winhausen et al. 2023). Pore pressure increase likely caused inelastic deformation of wet samples at lower differential stresses (Fig. 2) as well as reduced stresses at c_i, c_d and peak stress. Second, if the deformation rate is not sufficiently slow to allow pore pressure to equilibrate, a non-uniformly distributed effective stress may also reduce sample strength (e.g., Duda and Renner 2012; Amann and Vogelhuber 2015; Giger et al. 2018; Schuster et al. 2021, 2022). Third, capillary suction increases with decreasing water content, which leads to shrinkage and higher interparticle shear resistance, resulting in an increase of strength and stiffness (e.g., Wild et al. 2015; Zhang 2017; Yurikov et al. 2019). Fourth, water enhances the contribution of subcritical crack growth (Atkinson 1984) by adsorption effects at grain boundaries, reducing free surface energy of quartz and calcite (e.g., Rehbinder and Lichtman 1957; Parks 1984; Røyne et al. 2011) and water-assisted stress corrosion (e.g., Scholz 1972; Anderson and Grew 1977; Atkinson and Meredith 1981; Kranz et al. 1982). The latter reduces the stress required for crack initiation and may lead to yield stress and strength reduction of rocks (e.g., Rutter 1972; Rutter and Mainprice 1978; Baud et al. 2000; Heap et al. 2009; Nara et al. 2011; Brantut et al. 2013; Nicolas et al. 2016; Sari et al. 2022; Zega and Zhu 2023). Finally, the increased thickness of interlayer adsorbed and interparticle bound water of clay minerals in saturated samples reduces solid–solid grain contacts and facilitates interparticle motion and frictional sliding of clay minerals (e.g., Ikari et al. 2007, 2009; Zhang 2017).

Interestingly, we observe different volumetric deformation behavior of the saturated samples in both orientations beyond c_i. In p-orientation compaction dominates over dilation until peak strength is reached. In contrast, compaction decreases in s-orientation, resulting in pronounced dilation prior to peak stress. Under effectively undrained conditions (constant pore fluid mass), pore pressure changes are strongly controlled by the pore volume, with volumetric compaction leading to pore pressure generation and dilation (e.g. by microcracking) leading to pore pressure dissipation (e.g., Brace and Martin 1968; Islam and Skalle 2013; Wild and Amann 2018). The generation of pore pressure during axial deformation at constant confinement is expressed by the Skempton AB coefficient (Skempton 1954), giving the ratio between the change in pore pressure and differential stress. Consequently, the magnitude of the AB coefficient depends on the material's stiffness and is maximum at c_i, where dilatant microcracking initiates, while the generated pore pressure reaches a maximum at the onset of dilation c_d (e.g., Giger et al. 2018; Minardi et al. 2020). Therefore, it can be assumed that at undrained conditions, pore pressure generation due to clay matrix compaction is significantly higher for the more compliant s-sample ($AB >> 1/3$) in comparison to the p-sample ($AB < 1/3$), which is consistent with previous experimental studies, investigating the anisotropic hydro-mechanical behavior of OPA and other shales

(e.g., Islam and Skalle 2013; Giger et al. 2018; Wild and Amann 2018; Minardi et al. 2020; Winhausen et al. 2023). Accordingly, effective mean stress ($\sigma_{mean}' = (\sigma_1 + 2 \times p_c)/3 - p_f$) decreases at the beginning of differential loading in the s-sample to a minimum σ_{mean}' at c_i (maximum AB). Instead, shear-enhanced compaction dominates in the p-sample as the σ_{mean}' increases continuously with differential stress up to peak strength (Cuss et al. 2003; Giger et al. 2018; Minardi et al. 2020; Winhausen et al. 2023).

Ductile behavior of wet samples is likely accommodated by interparticle motion and frictional sliding of clay minerals. This is supported by the reduced number of recorded AE and high density of anastomosing shear bands (Fig. 5e, f), as observed for Callovo-Oxfordian Clay (Chiarelli et al. 2000; Zhang et al. 2012), Tournemire Shale (Valès et al. 2004) and Whitby Mudstone (Douma et al. 2019). However, strain hardening (predominantly in the s-sample), slow, stable faulting and delocalized deformation of wet samples in both orientations is presumably further enhanced by dilatancy hardening (Rice 1975; Duda and Renner 2012; Faulkner et al. 2018; Brantut 2021). Due to the low permeability and low hydraulic diffusivity of OPA (Philipp et al. 2017), it can be assumed that pore pressure at crack tips dropped significantly during propagation, increasing the effective pressure and thus stabilizing and/or inhibiting critical crack growth and interaction (e.g., Cook 1999; Duda and Renner 2012; Zega and Zhu 2023). A contribution of enhanced subcritical crack growth may be indicated by the pronounced velocity reduction of P-waves measured perpendicular to the stress axis (Fig. 7c, d).

Similar as previously observed in soils and shales (e.g., Hatibu and Hettiaratchi 1993; Chiarelli et al. 2000; Valès et al. 2004; Douma et al. 2019), our results demonstrate that observed weakening effects due to water saturation shift the brittle-ductile transition (Byerlee 1968) of Opalinus Clay to lower pressure.

4.2 Factors Controlling Stress-Induced Elastic Anisotropy Evolution of Shales

As discussed above, P-wave velocity and elastic anisotropy of sandy facies' OPA are sensitive to the degree of water saturation and to differential stress, its magnitude and direction relative to the bedding plane orientation (Fig. 7e, f). To better illustrate and interpret the velocity evolution of each sample during differential loading, we plotted P-wave velocity and propagation direction relative to bedding and stress orientation in 3D-space (Fig. 8). Assuming an ellipsoidal anisotropy of the three velocity traces covered by our sensor setup, we fitted the measured velocities in azimuthal and polar directions to an ellipse, which allows to estimate velocities for additional propagation angles that were not measured experimentally. In agreement with previous experimental studies performed on OPA of the shaly and sandy facies, as well as other different shale types (e.g., Dewhurst and Siggins 2006; Popp and Salzer 2007; Sarout et al. 2007; Sarout and Guéguen 2008; Delle Piane et al. 2011; Dewhurst et al. 2011; Kuila et al. 2011; Siegesmund et al. 2014; Bonnelye et al. 2017; Li et al. 2018; Douma et al. 2019), we observe increasing elastic wave anisotropy (Fig. 8a, b) in polar direction along the stress axis when bedding-parallel deformation is applied (perpendicular to the symmetry axis). Deformation parallel to the symmetry axis (normal to bedding) is leading to a reduction of elastic wave anisotropy in polar direction (Fig. 8 c, d). The increase of polar anisotropy in p-samples (Fig. 8a, b) is due to dilatancy parallel to bedding by opening of vertical microcracks perpendicular to the σ_1-direction. Crack opening significantly reduces P-wave propagation in radial direction but stress-parallel velocity ($\theta = 90°_{paral.}$) largely remains unaffected. In contrast to the interpretation of preferred microcrack opening along bedding, derived from radial strain measurements (Fig. 2a, b), the rather homogeneous decrease of radially measured P-wave velocities suggests microcrack opening also at other azimuthal directions (Fig. 3a, b). Therefore, differential loading of the sandy facies parallel to bedding alters the elastic symmetry from initial transverse isotropy presumably to an orthorhombic symmetry, as shown by the divergence of bedding parallel P-wave velocities measured at $\theta = 90°_{paral.}$ and $\theta = 90°_{perp.}$ (c.f., Delle Piane et al. 2011; Mayr et al. 2016; Bonnelye et al. 2017; Olsen-Kettle et al. 2022). This process is even more pronounced under saturated conditions, when the deformation is more ductile and delocalized (Fig. 7e).

Apart from the effects of stress (hydrostatic and differential) and water saturation on P-wave propagation and anisotropy in shales (c.f., Sayers 1999; Valès et al. 2004; Delle Piane et al. 2011; Bonnelye et al. 2017; Douma et al. 2019), mineral composition, organic content, porosity (and pore shape), burial history, maturity and diagenesis have also been found to significantly influence mechanical behavior and properties, as well as dynamic stiffness and elastic anisotropy (e.g., Vernik and Nur 1992; Vernik and Liu 1997; Vanorio et al. 2008; Sone and Zoback 2013a, b; Delle Piane et al. 2015; Rybacki et al. 2015; Herrmann et al. 2018).

In the following, we compile the results of experimental studies that measured P-wave velocities of shales during triaxial deformation parallel and perpendicular to the bedding orientation, in an attempt to highlight and discuss the aforementioned factors on the stress-dependent anisotropy of shales with respect to loading direction relative to microfabric orientation. Unfortunately, there are only a few experimental studies that measured the elastic wave velocities of shales deformed under triaxial conditions. Furthermore, as it is the case in this study, most experiments were

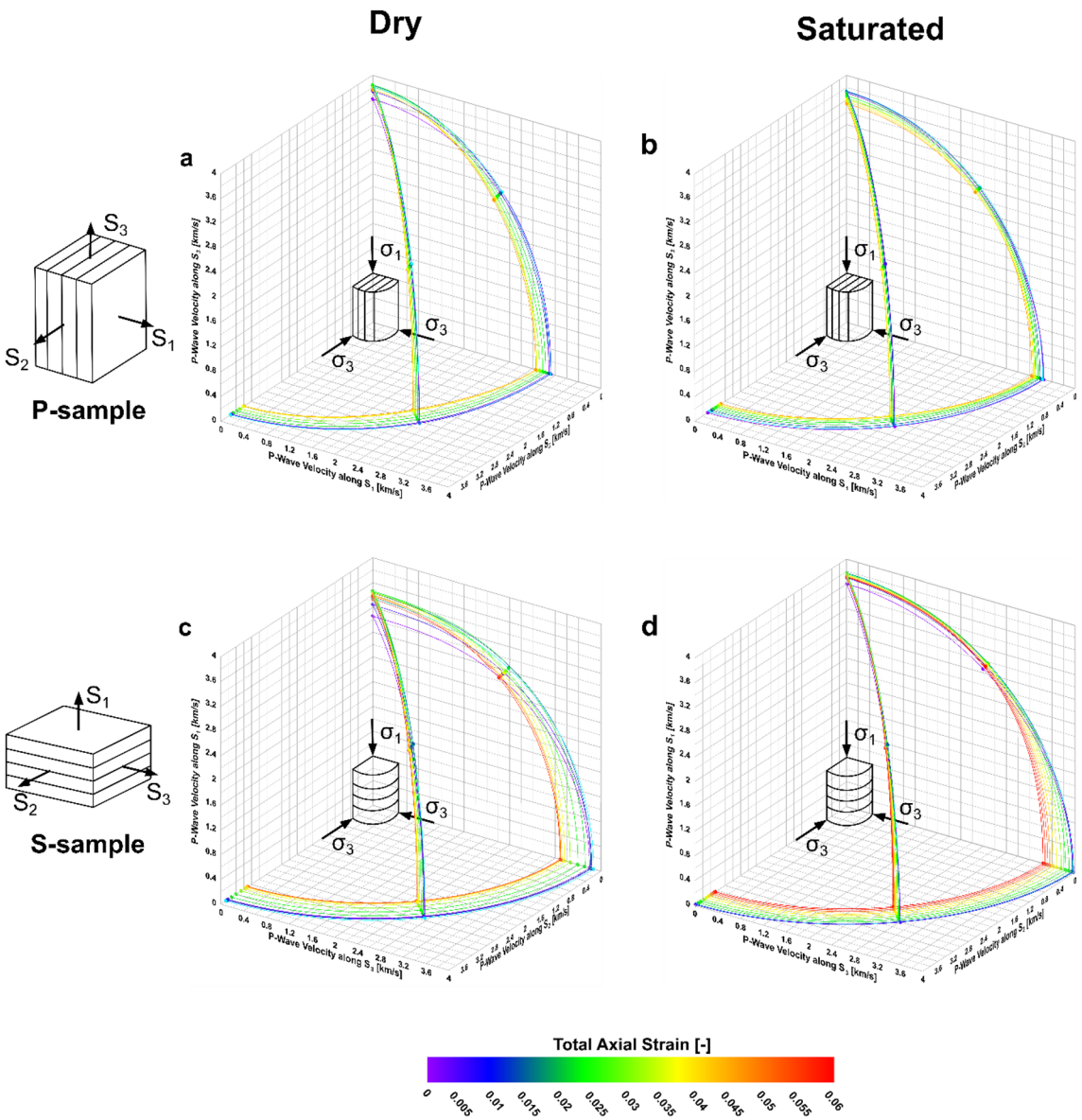

Fig. 8 Evolution of group P-wave velocities of the sandy facies of OPA propagating at different ray paths with respect to bedding orientation during differential loading at 50 MPa confining pressure. Elastic velocities (represented by dots) were measured at specific total axial strain (indicated by color bar) and were fit to an ellipse (shown by lines). For reasons of symmetry, only one octant is shown

conducted without controlling and monitoring pore pressure during loading. In these tests, effective stress state and the degree of saturation of the samples remain unknown, which complicates a direct comparison of elastic wave anisotropy between the different shales. These experiments include the results of OPA of the shaly and sandy facies (Popp and Salzer 2007; Siegesmund et al. 2014), Tournemire Shale (Bonnelye et al. 2017), Callovo-Oxfordian Clay (Sarout and Guéguen 2008), Whitby Mudstone (Douma et al. 2019) and Sichuan Basin Longmaxi Shale (Li et al. 2018). In all studies, dry, rewetted or partially saturated samples were deformed without quantification of pore pressure. On the other hand, the experimental studies of Dewhurst and Siggins 2006 (Muderong Shale), Delle Piane et al. 2011 (Northwest Shelf Shale), Dewhurst et al. 2011 (Norwegian Sea Shale), Kuila et al. 2011 (Officer Basin Shale) and Douma et al. 2019 (100% saturated Whitby Mudstone) report elastic wave velocities of fully saturated samples that quantify pore pressure evolution during deformation.

The investigated shales mostly comprise the same mineral constituents (determined by XRD analysis) composed of a mixture of quartz (Q), feldspars (F), pyrite (P), carbonates (Cb), clay and phyllosilicate minerals (Clay) and organic matter (TOC). Each component was converted from weight

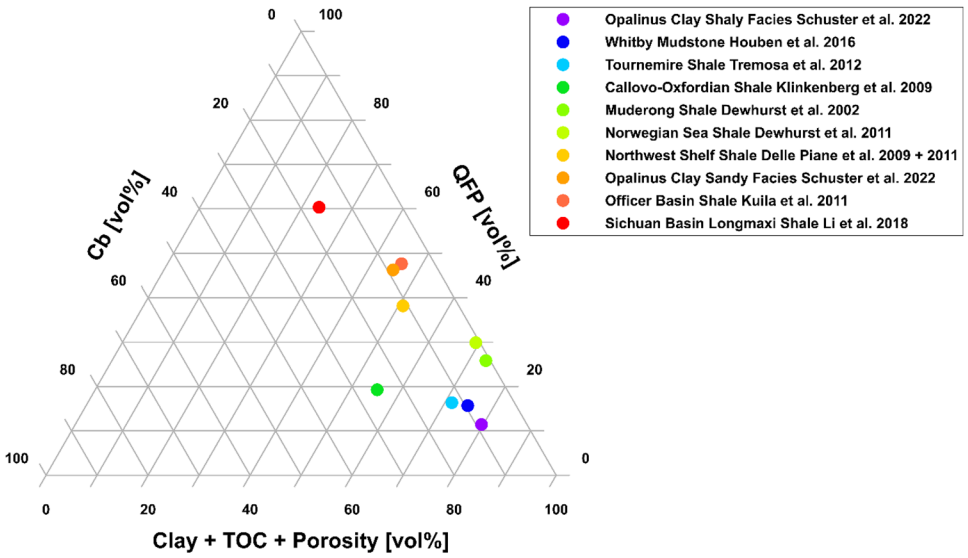

Fig. 9 Ternary diagram representing the mineral composition of ten different shales (see also Table 2 of the supporting material). Composition is normalized in vol% (including porosity) and separated into mechanically strong (QFP), intermediate (Cb) and weak (Clay + TOC + Porosity) fractions (see text for details)

(wt%) to volume percent (vol%) using the individual bulk density of each mineral phase according to Rybacki et al. (2015) and then renormalized accounting for porosity (see also Table 2 of the supporting material). Subsequently, the different compounds were grouped into three categories based on their contrasting mechanical properties. Accordingly, QFP refers to the strong phases comprising the volumetric sum of quartz, feldspars and pyrite, Cb are regarded as intermediate strong and include the fraction of the various carbonate phases (e.g., calcite, dolomite, siderite), and Clay + TOC + Porosity refers to the weakest phases and comprise all clay minerals (including mica), total organic carbon and porosity (c.f., Sone and Zoback 2013a, b; Rybacki et al. 2015; Herrmann et al. 2018).

Figure 9 shows the mineral composition of the selected shales, all of which have relatively low carbonate content (Cb < 30 vol%) and are rich in weak phases (Clay + TOC + Porosity > 40 vol%), except for the Longmaxi shale from the Sichuan Basin, which is richest in strong mineral phases (QFP≈60vol%). To compare the elastic anisotropy evolution of the individual shales during differential loading, we compiled P-wave velocities measured perpendicular and parallel to the bedding plane orientation and determined the P-wave anisotropy coefficient A_p as defined in Chapter 4.1. Since the compiled shales were deformed at different confining pressures, in Fig. 10a, b we plot A_p as a function total mean stress, neglecting pore pressure of wet, partially saturated or dried samples. In Fig. 10c, d A_p is given as a function of effective mean stress, assuming a Biot–Willis coefficient of 1, based on the data of Dewhurst and Siggins 2006 (Muderong Shale), Delle Piane et al. 2011 (Northwest Shelf Shale), Dewhurst et al. 2011 (Norwegian Sea Shale), Kuila et al. 2011 (Officer Basin Shale) and Douma et al. 2019 (100% saturated Whitby Mudstone).

In general, the evolution of P-wave anisotropy of the different shales during differential loading with respect to the orientation of the bedding planes is in good agreement with the results of the sandy facies of OPA obtained in this study. Thus, A_p in polar direction increases during differential loading of p-samples, whereas A_p measured in azimuthal direction remains constant or decreases slightly (Fig. 10a, c). On the other hand, A_p of s-samples decreases with increasing mean (effective) stress during axial deformation (Fig. 10b, d). The change in anisotropy coefficient due to the application of differential stress, as discussed in Chapter 4.1, can probably be explained by the opening of fractures predominantly aligned with the bedding planes in the case of p-samples and the compaction and closure of bedding-parallel fractures and pores combined with the formation of vertical stress-induced microcracks in s-samples. However, we observe that the initial anisotropy coefficient as well as its rate of change with increasing mean stress varies significantly between the different shale types.

For all examined shales, initial anisotropy generally decreases with increasing hydrostatic pressure due to porosity reduction and fracture closure as well as with increasing degree of water saturation. The absolute reduction in anisotropy during differential loading appears to decrease with increasing initial confining pressure and water saturation (especially in s-samples). As reported in previous studies (e.g., Vernik and Nur 1992; Vernik and Liu 1997; Sone and Zoback 2013a, b), we observe a strong correlation between the degree of anisotropy and mineral composition. The anisotropy coefficient of the different shales increases with increasing Clay + TOC + Porosity. This can be explained by the intrinsic anisotropy of clay minerals and their tendency, as well as of organic carbon, to align parallel to bedding, which results in decreasing stiffness and increasing

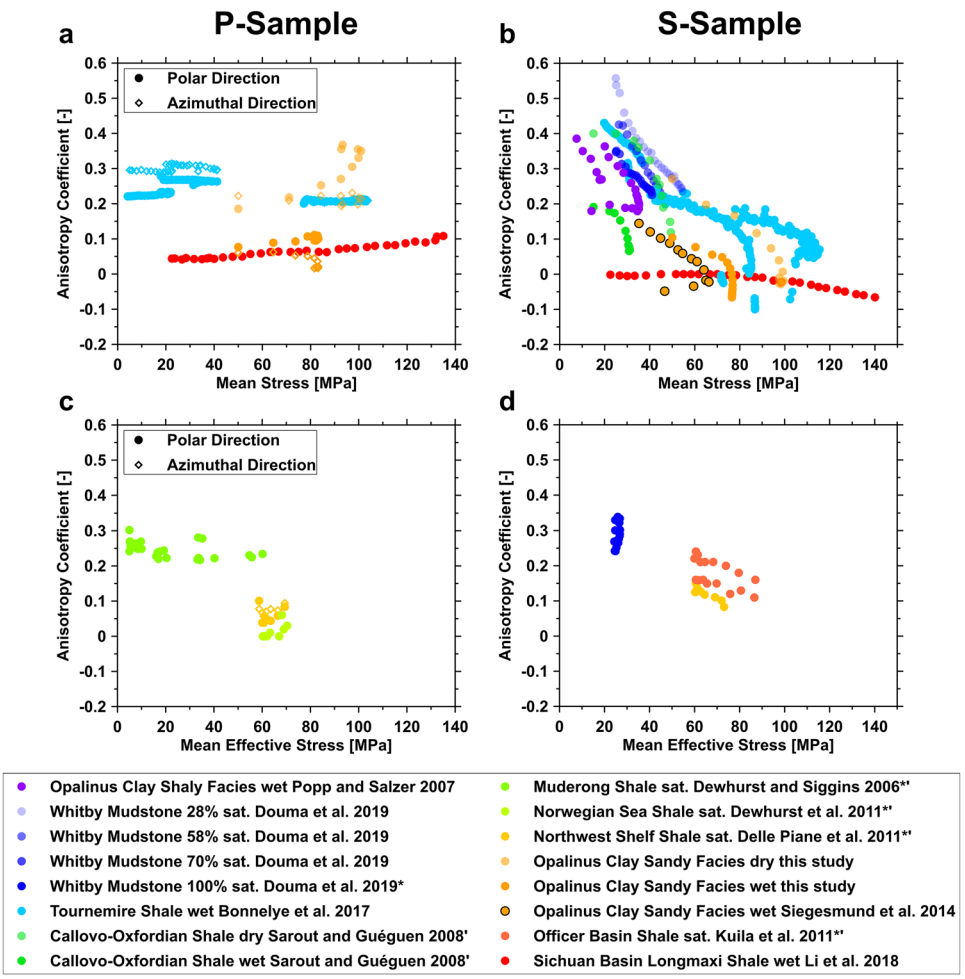

Fig. 10 Evolution of P-wave anisotropy coefficient of different shales as a function of total (**a**, **b**) and effective (**c**, **d**) mean stress. Samples were deformed parallel and perpendicular to bedding plane i.e., microfabric orientation at undrained conditions either dry, wet (partially saturated without pore pressure quantification) or fully saturated (sat.) with quantification of pore pressure and effective stress (marked with * in the legend). All samples were deformed up to failure either in single step experiments or after performing hydrostatic pressure cycles and multistage triaxial tests at different confining pressures (marked with ' in the legend)

anisotropy. Accordingly, QFP-rich shales such as Longmaxi and sandy facies OPA display lower initial anisotropy coefficients in comparison to shaly facies OPA or Whitby Mudstone that display a higher content of Clay + TOC + Porosity. This difference is likely due to the high quartz content of Longmaxi shale and sandy facies OPA (≥ 40wt%), which inhibits an alignment of phyllosilicates during diagenesis and reduces structural anisotropy (e.g., Wenk et al. 2008; Klinkenberg et al. 2009; Kaufhold et al. 2013; Sayers 2013; Siegesmund et al. 2014). Interestingly, anisotropy of organic-rich shales is further enhanced with increasing maturity, which suggests that not only the total volumetric proportion of clay or kerogen but also its thermal maturity, spatial microstructural fabric and diagenetic history determines elastic anisotropy (Vernik and Liu 1997; Vanorio et al. 2008; Sone and Zoback 2013a; Delle Piane et al. 2015). In addition, among the Clay + TOC + Porosity-rich shales, we observe large differences in the initial anisotropy. For example, the initial anisotropy coefficient of Norwegian Sea Shale is significantly lower than that of Tournemire or Muderong Shale at comparable mean stresses, although all three rocks have similar contents of weak mineral components (Fig. 9). The difference in anisotropy may be explained by the different contents of illite, smectite, chlorite and kaolinite of each shale, suggesting that apart from the total volumetric fraction of clay minerals, the dominant clay mineral type additionally influences anisotropy. For example, due to its lower intrinsic anisotropy (e.g., Sayers and den Boer 2016), kaolinite-rich shales (Northwest Shelf Shale, Norwegian Sea Shale) display lower elastic anisotropy than illite–smectite-rich shales (Muderong Shale, Tournemire Shale, Callovo-Oxfordian Clay, Whitby Mudstone). Additionally, the smaller grain size (clay and non-clay minerals) of the latter shales enhances elastic anisotropy as well as a stronger preferred orientation of elongated minerals (e.g., Hornby et al. 1998; Dewhurst and Siggins 2006; Delle Piane et al. 2011; Kuila et al. 2011).

Anisotropy reversal, as observed in s-samples in this study, was also reported by Siegesmund et al. 2014 (sandy facies of OPA), Bonnelye et al. 2017 (Tournemire Shale), and Li et al. 2018 (Longmaxi Shale) for samples that were deformed perpendicular to bedding orientation. Whether or not elastic anisotropy reversal occurs during differential loading perpendicular to the bedding planes seems to depend

on the initial confining pressure, mineral composition and porosity. With increasing hydrostatic pressure, initial anisotropy decreases due to porosity reduction. This effect is enhanced when a differential stress is applied perpendicular to bedding, as compliant porosity such as bedding-parallel cracks pores easily accommodate deformation by closure, resulting in an increase of bedding-perpendicular P-wave velocity ($V_{\theta = 0^\circ}$). The lower the initial anisotropy, the more likely an anisotropy reversal will occur during deformation. Formations with high initial anisotropy due to a high content of intrinsic anisotropic composites, i.e., clay minerals such as illite, may not exhibit an elastic anisotropy reversal. On the other hand, approaching sample failure, elastic anisotropy reduction in s-samples is further enhanced by the formation of microcracks that are generated sub-parallel to the stress axis, leading to a reduction of bedding-parallel P-wave velocity ($V_{\theta = 90^\circ}$). The reduction in P-wave velocity due to microcrack generation clearly depends on several factors, such as crack density and aperture, as well as the preferred crack-opening orientation with respect to the P-wave propagation direction (e.g., Lockner et al. 1977; Sayers and Kachanov 1995; Fortin et al. 2006; Barnhoorn et al. 2018). Consequently, stress-induced microcracks in QFP-rich shales can be more easily detected at a given seismic resolution due to the larger crack apertures and may also have a different compliance than cracks in clay-rich shales (e.g., Dewhurst and Siggins 2006; Dewhurst et al. 2011; Kuila et al. 2011).

Comparing the absolute changes in bedding-parallel and -perpendicular P-wave velocity of the different shales deformed perpendicular to bedding, it becomes clear that elastic anisotropy changes in QFP-rich shales (e.g., sandy facies of OPA) is induced by a higher relative contribution of microcracking ($V_{\theta = 90^\circ}$ reduction), whereas compaction of compliant bedding-parallel crack-like pores is the more dominant mechanism in clay-rich shales as the shaly facies of OPA (c.f., this study; Popp and Salzer 2007; Siegesmund et al. 2014). Similarly, the increase in elastic anisotropy in polar direction of p-samples during axial deformation (Fig. 10a) is larger in QFP-rich shales (Longmaxi Shale, sandy facies of OPA) than in clay-rich shales (e.g., Tournemire Shale), presumably due to larger fracture apertures. Finally, the pattern of microfractures in p-samples and consequently elastic anisotropy evolution during the application of differential stress are affected by mineralogy, diagenesis, intensity of the pre-existing microstructural fabric (lamination and preferential alignment of minerals) and confinement. Due to a lower fracture toughness of the samples oriented parallel to bedding, an increase of elastic anisotropy of p-samples in polar direction is expected if the majority of pre-existing and newly generated microcracks open within the bedding planes of the shale in tensile mode as differential stress increases (e.g., Sayers and Kachanov 1995; Dewhurst et al. 2011). Accordingly, changes in elastic anisotropy seem to increase when the shale samples fail brittle, i.e., at low confining pressure and when dried before deformation, whereas absolute anisotropy changes reduce with increasing confinement or saturation, favoring shear failure as well as delocalized, ductile deformation (c.f., sandy facies OPA and Tournemire Shale in Fig. 10).

Our observations emphasize that elastic anisotropy of shales depends on its compaction history, clay mineral composition, failure mode as well as on the magnitude and orientation of the stress regime relative to the microfabric/bedding orientation and should be considered when estimating velocity anisotropy for seismic interpretations. Furthermore, it becomes evident that the elastic symmetry of initially transversely isotropic shales may be significantly altered in an anisotropic stress field, which is primarily controlled by the interplay between stress-induced closure and opening of microcracks and pores.

5 Conclusion

In this study, we report on undrained triaxial deformation tests combined with monitoring of ultrasonic P-wave velocities and AE performed on p- and s-samples of the sandy facies of OPA. The experiments were designed to investigate the effect of water on the mechanical properties, dynamic elastic anisotropy and failure behavior at a confining pressure of 50 MPa. Dry samples display semi-brittle deformation behavior, whereas wet samples exhibit increasingly delocalized (ductile) deformation and stable faulting. The mechanical properties and deformation behavior of wet samples are significantly influenced by anisotropic hydro-mechanical coupling. Compressive strength, P-wave velocity, Young's modulus and Poisson's ratio depend on bedding plane orientation as well as water saturation. Peak strengths and Poisson's ratios of dry p- and s-samples are almost identical, whereas P-wave velocity and Young's modulus are highest parallel to the bedding plane and lowest perpendicular to it. Initial P-wave velocity anisotropy, stress at the onset of microcracking, peak strength and Young's modulus are drastically reduced for wet samples, whereas Poisson's ratio increases. Apart from poroelastic effects, delocalization, stable faulting and weakening are likely to be induced by the presence of water and facilitated by frictional sliding of phyllosilicates and a combination of subcritical crack growth and dilatant hardening.

By determination of P-wave velocities along different propagation paths through the sample, we were able to characterize changes in the P-wave velocity anisotropy of the sandy facies during deformation. For wet and dry s-samples, we observed a reduction and reversal of the

initial anisotropy during loading. This is attributed to the simultaneous compaction of bedding-parallel pores and generation of microcracks, leading to a P-velocity increase perpendicular to bedding and a velocity reduction parallel to bedding. In contrast, transverse isotropy of p-samples is eliminated during loading, while elastic anisotropy in polar direction is increased due to favored opening of bedding planes. Initial P-wave anisotropy is reduced for wet samples in both orientations. P-wave velocities are more sensitive to strain accumulation by dilatant microcracking and compaction of porosity than to mineral reorientation induced by shear zone formation. Our results demonstrate that the elastic symmetry of sandy facies OPA can be significantly altered in an anisotropic stress field, highlighting the influence of the orientation of the pre-existing microfabric relative to the maximum principal stress. This implies that the elastic properties and anisotropy of rocks in the vicinity of zones of high stress gradients (e.g., fault zones or underground excavations) may vary considerably compared to the undisturbed host rock and change as a function of distance to them.

Supplementary Information The online version contains supplementary material available at https://doi.org/10.1007/s00603-024-03802-z.

Acknowledgements The authors acknowledge the financial support for the iCross project by the Federal Ministry of Education and Research (project number 02NUK053D), the Helmholtz Association (project number SO-093) and the GFZ German Research Centre for Geosciences Potsdam. We would like to thank Michael Naumann for his technical support during the experiments and Stefan Gehrmann for sample preparation. Furthermore, we thank David Jaeggi, Thierry Theurillat and Senecio Schefer for providing samples of Opalinus Clay. Finally, we are grateful for the constructive comments of two anonymous reviewers, which improved the quality of the manuscript.

Funding Open Access funding enabled and organized by Projekt DEAL.

Data Availability Data availability on request.

Code Availability Not applicable.

Declarations

Conflict of Interest The authors declare that they have no conflict of interest.

References

Amann F, Button EA, Evans KF, Gischig VS, Blumel M (2011) Experimental study of the brittle behavior of clay shale in rapid unconfined compression. Rock Mech Rock Eng 44(4):415–430. https://doi.org/10.1007/s00603-011-0156-3

Amann F, Vogelhuber M (2015). Assessment of geomechanical properties of intact opalinus clay. Unpublished expert report ENSI, 33, p 461

Anderson OL, Grew PC (1977) Stress corrosion theory of crack propagation with applications to geophysics. Rev Geophys 15(1):77–104. https://doi.org/10.1029/RG015i001p00077

Atkinson BK (1984) Subcritical crack growth in geological materials. J Geophys Res 89(B6):4077–4114. https://doi.org/10.1029/JB089iB06p04077

Atkinson BK, Meredith PG (1981) Stress corrosion cracking of quartz: a note on the influence of chemical environment. Tectonophysics 77(1):T1–T11. https://doi.org/10.1016/0040-1951(81)90157-8

Barnhoorn A, Verheij J, Frehner M, Zhubayev A, Houben M (2018) Experimental identification of the transition from elasticity to inelasticity from ultrasonic attenuation analyses. Geophysics 83(4):MR221–MR229. https://doi.org/10.1190/geo2017-0534.1

Baud P, Zhu W, Wong T-F (2000) Failure mode and weakening effect of water on sandstone. J Geophys Res 105(B7):16371–16389. https://doi.org/10.1029/2000JB900087

Bernabé Y, Brace WF (1990) Deformation and fracture of Berea sandstone. In: The brittle–ductile transition in rocks, pp 91–101

Berthé D, Choukroune P, Jegouzo P (1979) Orthogneiss, mylonite and noncoaxial deformation of granites: the example of the South Armorican Shear Zone. J Struct Geol 1(1):31–42. https://doi.org/10.1016/0191-8141(79)90019-1

BGE (2022) Zwischenbericht Teilgebiete gemäß § 13 StandAG. https://www.bge.de/de/endlagersuche/zwischenbericht-teilgebiete/, 02.10.2022, Bundesgesellschaft für Endlagerung mbH (BGE), Peine, Germany

Boness NL, Zoback MD (2006) Mapping stress and structurally controlled crustal shear velocity anisotropy in California. Geology 34(10):825–828. https://doi.org/10.1130/g22309.1

Bonnelye A, Schubnel A, David C, Henry P, Guglielmi Y, Gout C, . . . Dick P (2017) Elastic wave velocity evolution of shales deformed under uppermost crustal conditions. J Geophys Res Solid Earth 122(1):130–141. https://doi.org/10.1002/2016jb013540

Bossart P, Meier PM, Moeri A, Trick T, Mayor J-C (2002) Geological and hydraulic characterisation of the excavation disturbed zone in the Opalinus Clay of the Mont Terri Rock Laboratory. Eng Geol 66(1):19–38. https://doi.org/10.1016/S0013-7952(01)00140-5

Bossart P, Bernier F, Birkholzer J, Bruggeman C, Connolly P, Dewonck S, . . . Wieczorek K (2017). Mont Terri rock laboratory, 20 years of research: introduction, site characteristics and overview of experiments. Swiss J Geosci 110(1):3–22. https://doi.org/10.1007/s00015-016-0236-1

Bourg IC (2015) Sealing shales versus brittle shales: a sharp threshold in the material properties and energy technology uses of fine-grained sedimentary rocks. Environ Sci Technol Lett 2(10):255–259. https://doi.org/10.1021/acs.estlett.5b00233

Brace WF, Martin RJ (1968) A test of the law of effective stress for crystalline rocks of low porosity. Int J Rock Mech Min Sci Geomech Abstracts 5(5):415–426. https://doi.org/10.1016/0148-9062(68)90045-4

Brantut N, Heap MJ, Meredith PG, Baud P (2013) Time-dependent cracking and brittle creep in crustal rocks: a review. J Struct Geol 52:17–43. https://doi.org/10.1016/j.jsg.2013.03.007

Brantut N (2021) Dilatancy Toughening of Shear Cracks and Implications for Slow Rupture Propagation. J Geophys Res

126(11):e2021JB022239. https://doi.org/10.1029/2021JB022239

Byerlee JD (1968) Brittle-ductile transition in rocks. J Geophys Res (1896–1977) 73(14), 4741–4750. https://doi.org/10.1029/JB073i014p04741

Carpinteri A, Corrado M, Lacidogna G (2013) Heterogeneous materials in compression: correlations between absorbed, released and acoustic emission energies. Eng Fail Anal 33:236–250. https://doi.org/10.1016/j.engfailanal.2013.05.016

Carpinteri A, Lacidogna G, Corrado M, Di Battista E (2016) Cracking and crackling in concrete-like materials: a dynamic energy balance. Eng Fract Mech 155:130–144. https://doi.org/10.1016/j.engfracmech.2016.01.013

Chiarelli A-S, Ledesert B, Sibai M, Karami M, Hoteit N (2000) Influence of mineralogy and moisture content on plasticity and induced anisotropic damage of a claystone; application to nuclear waste disposals. Bull De La Société Géologique De France 171(6):621–627. https://doi.org/10.2113/171.6.621

Cook J (1999) The Effects of Pore Pressure on the Mechanical and Physical Properties of Shales. Oil & Gas Science and Technology - Revue d'IFPEN 54(6):695–701. https://doi.org/10.2516/ogst:1999059

Crampin S, Chesnokov EM, Hipkin RG (1984) Seismic anisotropy—the state of the art: II. Geophys J Int 76(1):1–16. https://doi.org/10.1111/j.1365-246X.1984.tb05017.x

Crisci E, Ferrari A, Giger SB, Laloui L (2019) Hydro-mechanical behaviour of shallow Opalinus Clay shale. Eng Geol 251:214–227. https://doi.org/10.1016/j.enggeo.2019.01.016

Cui YJ, Delage P (1996) Yielding and plastic behaviour of an unsaturated compacted silt. Geotechnique 46(2):291–311. https://doi.org/10.1680/geot.1996.46.2.291

Cuss RJ, Rutter EH, Holloway RF (2003) The application of critical state soil mechanics to the mechanical behaviour of porous sandstones. Int J Rock Mech Min Sci 40(6):847–862. https://doi.org/10.1016/S1365-1609(03)00053-4

Delle Piane C, Dewhurst DN, Siggins AF, Raven MD (2011) Stress-induced anisotropy in brine saturated shale. Geophys J Int 184(2):897–906. https://doi.org/10.1111/j.1365-246X.2010.04885.x

Delle Piane C, Almqvist BSG, MacRae CM, Torpy A, Mory AJ, Dewhurst DN (2015) Texture and diagenesis of Ordovician shale from the Canning Basin, Western Australia: Implications for elastic anisotropy and geomechanical properties. Mar Pet Geol 59:56–71. https://doi.org/10.1016/j.marpetgeo.2014.07.017

Delle Piane C, Dewhurst D, Siggins A, Raven M (2009) Geomechanical and rock physics properties of an Australian Northwest shelf shale. In: SEG technical program expanded abstracts 2009, pp 2213–2217

Dellinger J, Vernik L (1994) Do traveltimes in pulse-transmission experiments yield anisotropic group or phase velocities? Geophysics 59(11):1774–1779. https://doi.org/10.1190/1.1443564

Dewhurst DN, Siggins AF (2006) Impact of fabric, microcracks and stress field on shale anisotropy. Geophys J Int 165(1):135–148. https://doi.org/10.1111/j.1365-246X.2006.02834.x

Dewhurst DN, Jones RM, Raven MD (2002) Microstructural and petrophysical characterization of Muderong Shale: application to top seal risking. Pet Geosci 8(4):371–383. https://doi.org/10.1144/petgeo.8.4.371

Dewhurst DN, Siggins AF, Sarout J, Raven MD, Nordgård-Bolås HM (2011) Geomechanical and ultrasonic characterization of a Norwegian Sea shale. Geophysics 76(3):WA101–WA111. https://doi.org/10.1190/1.3569599

Douma LANR, Dautriat J, Sarout J, Dewhurst DN, Barnhoorn A (2019) Impact of water saturation on the elastic anisotropy of the Whitby Mudstone, United Kingdom. Geophysics 85(1):MR57–MR72. https://doi.org/10.1190/geo2019-0004.1

Dresen G, Evans B (1993) Brittle and semibrittle deformation of synthetic marbles composed of two phases. J Geophys Res 98(B7):11921–11933. https://doi.org/10.1029/93jb00697

Duda M, Renner J (2012) The weakening effect of water on the brittle failure strength of sandstone. Geophys J Int 192:1091-–1108. https://doi.org/10.1093/gji/ggs090

Esefelder R, Wawerzinek B, Lüth S, Giese R, Krawczyk CM (2021) Seismic anisotropy of Opalinus Clay: tomographic investigations using the infrastructure of an underground rock laboratory (URL). Swiss J Geosci 114(1):21. https://doi.org/10.1186/s00015-021-00398-2

Evans B, Fredrich JT, Wong TF (1990) The brittle-ductile transition in rocks: recent experimental and theoretical progress. In: The brittle-ductile transition in rocks, pp 1–20

Faulkner DR, Sanchez-Roa C, Boulton C, den Hartog SAM (2018) Pore fluid pressure development in compacting fault gouge in theory, experiments, and nature. J Geophys Res 123(1):226–241. https://doi.org/10.1002/2017JB015130

Favero V, Ferrari A, Laloui L (2018) Anisotropic behaviour of opalinus clay through consolidated and drained triaxial testing in saturated conditions. Rock Mech Rock Eng 51(5):1305–1319. https://doi.org/10.1007/s00603-017-1398-5

Ferrari A, Favero V, Marschall P, Laloui L (2014) Experimental analysis of the water retention behaviour of shales. Int J Rock Mech Min Sci 72:61–70. https://doi.org/10.1016/j.ijrmms.2014.08.011

Fortin J, Stanchits S, Dresen G, Guéguen Y (2006) Acoustic emission and velocities associated with the formation of compaction bands in sandstone. J Geophys Res 111(B10). https://doi.org/10.1029/2005JB003854

Fossen H, Cavalcante GCG (2017) Shear zones—a review. Earth Sci Rev 171:434–455. https://doi.org/10.1016/j.earscirev.2017.05.002

Ghorbani A, Zamora M, Cosenza P (2009) Effects of desiccation on the elastic wave velocities of clay-rocks. Int J Rock Mech Min Sci 46(8):1267–1272. https://doi.org/10.1016/j.ijrmms.2009.01.009

Giger SB, Ewy RT, Favero V, Stankovic R, Keller LM (2018) Consolidated-undrained triaxial testing of opalinus clay: results and method validation. Geomech Energy Environ 14:16–28. https://doi.org/10.1016/j.gete.2018.01.003

Giger S, Marschall P (2014) Geomechanical properties, rock models and in-situ stress conditions for Opalinus Clay in Northern Switzerland. Nagra Arbeitsbericht NAB 14–01. Nagra, Wettingen.

Goebel THW, Becker TW, Schorlemmer D, Stanchits S, Sammis C, Rybacki E, Dresen G (2012) Identifying fault heterogeneity through mapping spatial anomalies in acoustic emission statistics. J Geophys Res Solid Earth 117:B03310. https://doi.org/10.1029/2011JB008763

Grosse C, Reinhardt H, Dahm T (1997) Localization and classification of fracture types in concrete with quantitative acoustic emission measurement techniques. NDT and E Int 30(4):223–230. https://doi.org/10.1016/S0963-8695(96)00060-6

Gutierrez M, Vik G, Berre T (1996) Shale strength as function of stress history and diagenesis. Paper presented at the ISRM International Symposium—EUROCK 96, Turin—Italy

Hatibu N, Hettiaratchi DRP (1993) The transition from ductile flow to brittle failure in unsaturated soils. J Agric Eng Res 54(4):319–328. https://doi.org/10.1006/jaer.1993.1024

Hawkins AB, McConnell BJ (1992) Sensitivity of sandstone strength and deformability to changes in moisture content. Q J Eng Geol 25(2):115–130. https://doi.org/10.1144/GSL.QJEG.1992.025.02.05

Heap MJ, Baud P, Meredith PG (2009) Influence of temperature on brittle creep in sandstones. Geophys Res Lett 36(19). https://doi.org/10.1029/2009gl039373

Herrmann J, Rybacki E, Sone H, Dresen G (2018) Deformation Experiments on Bowland and Posidonia Shale—Part I: strength and Young's modulus at ambient and in situ pc–T conditions. Rock Mech Rock Eng 51(12):3645–3666. https://doi.org/10.1007/s00603-018-1572-4

Hornby BE (1998) Experimental laboratory determination of the dynamic elastic properties of wet, drained shales. J Geophys Res 103(B12):29945–29964. https://doi.org/10.1029/97JB02380

Hostettler B, Reisdorf AG, Jaeggi D, Deplazes G, Bläsi H, Morard A, . . . Menkveld-Gfeller U (2017) Litho- and biostratigraphy of the opalinus clay and bounding formations in the Mont terri rock laboratory (Switzerland). Swiss J Geosci 110(1):23–37. https://doi.org/10.1007/s00015-016-0250-3

Hoth P, Wirth H, Reinhold K, Bräuer V, Krull P, Feldrappe H (2007) Endlagerung radioaktiver Abfälle in tiefen geologischen Formationen Deutschlands–Untersuchung und Bewertung von Tongesteinsformationen. BGR Bundesanstalt für Geowissenschaften und Rohstoffe, Hannover/Germany

Houben ME, Desbois G, Urai JL (2013) Pore morphology and distribution in the Shaly facies of Opalinus Clay (Mont Terri, Switzerland): Insights from representative 2D BIB–SEM investigations on mm to nm scale. Appl Clay Sci 71:82–97. https://doi.org/10.1016/j.clay.2012.11.006

Houben ME, Desbois G, Urai JL (2014) A comparative study of representative 2D microstructures in Shaly and Sandy facies of Opalinus Clay (Mont Terri, Switzerland) inferred form BIB-SEM and MIP methods. Mar Pet Geol 49:143–161. https://doi.org/10.1016/j.marpetgeo.2013.10.009

Houben ME, Barnhoorn A, Lie-A-Fat J, Ravestein T, Peach CJ, Drury MR (2016) Microstructural characteristics of the Whitby Mudstone Formation (UK). Mar Pet Geol 70:185–200. https://doi.org/10.1016/j.marpetgeo.2015.11.011

Ibanez WD, Kronenberg AK (1993) Experimental deformation of shale - mechanical-properties and microstructural indicators of mechanisms. Int J Rock Mech Min Sci Geomech Abstracts 30(7):723–734. https://doi.org/10.1016/0148-9062(93)90014-5

Ikari MJ, Saffer DM, Marone C (2007) Effect of hydration state on the frictional properties of montmorillonite-based fault gouge. J Geophys Res 112(B6). https://doi.org/10.1029/2006JB004748

Ikari MJ, Saffer DM, Marone C (2009) Frictional and hydrologic properties of clay-rich fault gouge. Journal of Geophysical Research: Solid Earth, 114(B5). https://doi.org/10.1029/2008JB006089

Ingram GM, Urai JL (1999) Top-seal leakage through faults and fractures: the role of mudrock properties. Geol Soc London Spec Publ 158:125–135

Islam MA, Skalle P (2013) An experimental investigation of shale mechanical properties through drained and undrained test mechanisms. Rock Mech Rock Eng 46(6):1391–1413. https://doi.org/10.1007/s00603-013-0377-8

Jaeger JC, Cook NGW, Zimmerman RW (2007) Fundamentals of rock mechanics, 4th edn. Blackwell, Oxford, Malden, Mass

John H, Hager RV Jr, Friedman M, Feather JN (1963) Experimental deformation of sedimentary rocks under confining pressure: pore pressure tests. AAPG Bull 47(5):717–755. https://doi.org/10.1306/bc743a87-16be-11d7-8645000102c1865d

Johnston JE, Christensen NI (1995) Seismic anisotropy of shales. J Geophys Res 100(B4):5991–6003. https://doi.org/10.1029/95JB00031

Kaufhold A, Grasle W, Plischke I, Dohrmann R, Siegesmund S (2013) Influence of carbonate content and micro fabrics on the failure strength of the sandy facies of the Opalinus Clay from Mont Terri (Underground Rock Laboratory). Eng Geol 156:111–118. https://doi.org/10.1016/j.enggeo.2013.01.014

Klinkenberg M, Kaufhold S, Dohrmann R, Siegesmund S (2009) Influence of carbonate microfabrics on the failure strength of claystones. Eng Geol 107(1):42–54. https://doi.org/10.1016/j.enggeo.2009.04.001

Kneuker T, Furche M (2021) Capturing the structural and compositional variability of Opalinus Clay: constraints from multidisciplinary investigations of Mont Terri drill cores (Switzerland). Environ Earth Sci 80(11):421. https://doi.org/10.1007/s12665-021-09708-1

Kranz RL, Harris WJ, Carter NL (1982) Static fatigue of granite at 200°C. Geophys Res Lett 9(1):1–4. https://doi.org/10.1029/GL009i001p00001

Kuila U, Dewhurst DN, Siggins AF, Raven MD (2011) Stress anisotropy and velocity anisotropy in low porosity shale. Tectonophysics 503(1):34–44. https://doi.org/10.1016/j.tecto.2010.09.023

Kwiatek G, Charalampidou E-M, Dresen G, Stanchits S (2014) An improved method for seismic moment tensor inversion of acoustic emissions through assessment of sensor coupling and sensitivity to incidence angle. Int J Rock Mech Min Sci 65:153–161. https://doi.org/10.1016/j.ijrmms.2013.11.005

Laloui L, Salager S, Rizzi M (2013) Retention behaviour of natural clayey materials at different temperatures. Acta Geotech 8(5):537–546. https://doi.org/10.1007/s11440-013-0255-2

Lauper B, Jaeggi D, Deplazes G, Foubert A (2018) Multi-proxy facies analysis of the Opalinus Clay and depositional implications (Mont Terri rock laboratory, Switzerland). Swiss J Geosci 111(3):383–398. https://doi.org/10.1007/s00015-018-0303-x

Lauper B, Zimmerli GN, Jaeggi D, Deplazes G, Wohlwend S, Rempfer J, Foubert A (2021) Quantification of lithological heterogeneity within Opalinus clay: toward a uniform subfacies classification scheme using a novel automated core image recognition tool. Front Earth Sci 9(313). https://doi.org/10.3389/feart.2021.645596

Li X, Lei X, Li Q (2018) Response of Velocity Anisotropy of Shale Under Isotropic and Anisotropic Stress Fields. Rock Mech Rock Eng 51(3):695–711. https://doi.org/10.1007/s00603-017-1356-2

Lisjak A, Garitte B, Grasselli G, Müller HR, Vietor T (2015) The excavation of a circular tunnel in a bedded argillaceous rock (Opalinus Clay): Short-term rock mass response and FDEM numerical analysis. Tunn Undergr Space Technol 45:227–248. https://doi.org/10.1016/j.tust.2014.09.014

Lockner D (1993) The role of acoustic emission in the study of rock fracture. Int J Rock Mech Min Sci Geomech Abstracts 30(7):883–899. https://doi.org/10.1016/0148-9062(93)90041-B

Lockner D (1998) A generalized law for brittle deformation of Westerly granite. J. Geophys. Res. Solid Earth 103:5107–5123. https://doi.org/10.1029/97JB03211

Lockner DA, Walsh JB, Byerlee JD (1977) Changes in seismic velocity and attenuation during deformation of granite. J Geophys Res (1896–1977) 82(33):5374–5378. https://doi.org/10.1029/JB082i033p05374

Lozovyi S, Bauer A (2019) Static and dynamic stiffness measurements with Opalinus Clay. Geophys Prospect 67(4):997–1019. https://doi.org/10.1111/1365-2478.12720

Martin RJ III (1980) Pore pressure stabilization of failure in westerly granite. Geophys Res Lett 7(5):404–406. https://doi.org/10.1029/GL007i005p00404

Masri M, Sibai M, Shao JF, Mainguy M (2014) Experimental investigation of the effect of temperature on the mechanical behavior of Tournemire shale. Int J Rock Mech Min Sci 70:185–191. https://doi.org/10.1016/j.ijrmms.2014.05.007

Mayr SI, Niemann R, Shapiro SA (2016) Understanding of elastic anisotropy of shale under triaxial loading: porosity-deformation approach. Geophysics 81(5):C163–C175. https://doi.org/10.1190/geo2015-0423.1

Minardi A, Crisci E, Ferrari A, Laloui L (2016) Anisotropic volumetric behaviour of Opalinus clay shale upon suction variation. Géotech Lett 6:144–148. https://doi.org/10.1680/jgele.16.00023

Minardi A, Giger SB, Ewy RT, Stankovic R, Stenebråten J, Soldal M, Laloui L (2020) Benchmark study of undrained triaxial testing of Opalinus Clay shale: Results and implications for robust testing. Geomech Energy Environ 100210. https://doi.org/10.1016/j.gete.2020.100210

Moore DE, Lockner DA (2004) Crystallographic controls on the frictional behavior of dry and water-saturated sheet structure minerals. J Geophys Res 109(B3). https://doi.org/10.1029/2003jb002582

Morrow CA, Moore DE, Lockner DA (2017) Frictional strength of wet and dry montmorillonite. J Geophys Res Solid Earth 122:3392–3409. https://doi.org/10.1002/2016JB013658

NAGRA (2002) Projekt Opalinuston - Synthese der geowissenschaftlichen Untersuchungsergebnisse (Vol. NTB 02–03): Nagra, Wettingen, Switzerland.

Nagra (2022) DER STANDORT FÜR DAS TIEFENLAGER. Der Vorschlag der Nagra. Report of the National Cooperative for the Disposal of Radioactive Waste. Nagra, Wettingen, Switzerland. https://nagra.ch/wp-content/uploads/2022/09/Bericht-zum-Standortvorschlag_D_Druckversion.pdf

Nara Y, Morimoto K, Yoneda T, Hiroyoshi N, Kaneko K (2011) Effects of humidity and temperature on subcritical crack growth in sandstone. Int J Solids Struct 48(7):1130–1140. https://doi.org/10.1016/j.ijsolstr.2010.12.019

Niandou H, Shao JF, Henry JP, Fourmaintraux D (1997) Laboratory investigation of the behaviour of Tournemire shale. Int J Rock Mech Min Sci 34(1):3–16. https://doi.org/10.1016/S0148-9062(96)00053-8

Nicolas A, Fortin J, Regnet JB, Dimanov A, Guéguen Y (2016) Brittle and semi-brittle behaviours of a carbonate rock: influence of water and temperature. Geophys J Int 206(1):438–456. https://doi.org/10.1093/gji/ggw154

Nicollin F, Gibert D, Bossart P, Nussbaum C, Guervilly C (2008) Seismic tomography of the excavation damaged zone of the gallery 04 in the Mont Terri rock laboratory. Geophys J Int 172(1):226–239. https://doi.org/10.1111/j.1365-246X.2007.03615.x

Nüesch R (1991) Das mechanische Verhalten von Opalinuston. ETH Zurich 9349, Diss, Switzerland

Nygård R, Gutierrez M, Gautam R, Høeg K (2004) Compaction behavior of argillaceous sediments as function of diagenesis. Mar Pet Geol 21(3):349–362. https://doi.org/10.1016/j.marpetgeo.2004.01.002

Olsen-Kettle L, Dautriat J, Sarout J (2022) Impact of stress-induced rock damage on elastic symmetry: from transverse isotropy to orthotropy. Rock Mech Rock Eng 55(6):3061–3081. https://doi.org/10.1007/s00603-022-02812-z

Parks GA (1984) Surface and interfacial free energies of quartz. J Geophys Res 89(B6):3997–4008. https://doi.org/10.1029/JB089iB06p03997

Paterson MS, Wong T-F (2005) Experimental rock deformation-the brittle field: Springer Science & Business Media.

Paul B, Royston KJ, Li Y, Stoll ML, Skibola CF, Wilson LS, Tollefsbol TO (2017) Impact of genistein on the gut microbiome of humanized mice and its role in breast tumor inhibition. Plos One, 12(12), e0189756. https://doi.org/10.1371/journal.pone.0189756

Pearson FJ, Arcos D, Bath D, Boisson JY, Fernández AM, Gäbler H-E, Waber HN (2003) Mont Terri project: geochemistry of water in the opalinus clay formation at the Mont Terri rock laboratory. Reports of the Federal Office for Water and Geology (FOWG), Geology Series No. 5.

Peron H, Hueckel T, Laloui L, Hu LB (2009) Fundamentals of desiccation cracking of fine-grained soils: experimental characterisation and mechanisms identification. Can Geotech J 46(10):1177–1201. https://doi.org/10.1139/t09-054

Pham QT, Vales F, Malinsky L, Nguyen Minh D, Gharbi H (2007) Effects of desaturation–resaturation on mudstone. Phys Chem Earth Parts A/B/C 32:646–655. https://doi.org/10.1016/j.pce.2006.03.012

Philipp T, Amann-Hildenbrand A, Laurich B, Desbois G, Littke R, Urai J (2017) The effect of microstructural heterogeneity on pore size distribution and permeability in Opalinus Clay (Mont Terri, Switzerland): insights from an integrated study of laboratory fluid flow and pore morphology from BIB-SEM images. Geol Soc Lond Spec Publ 454(1):85–106

Popp T, Salzer K (2007) Anisotropy of seismic and mechanical properties of Opalinus clay during triaxial deformation in a multi-anvil apparatus. Phys Chem Earth 32(8–14):879–888. https://doi.org/10.1016/j.pce.2006.04.022

Ramos da Silva M, Schroeder C, Verbrugge J-C (2008) Unsaturated rock mechanics applied to a low-porosity shale. Eng Geol 97(1):42–52. https://doi.org/10.1016/j.enggeo.2007.12.003

Rehbinder P, Lichtman V (1957) Effect of surface active media on strain and rupture in solids. Paper presented at the Proceedings of the Second International Congress of Surface Activity

Rice JR (1975) On the stability of dilatant hardening for saturated rock masses. J Geophys Res (1896–1977) 80(11):1531–1536. https://doi.org/10.1029/JB080i011p01531

Røyne A., Bisschop J, Dysthe DK (2011) Experimental investigation of surface energy and subcritical crack growth in calcite. J Geophys Res 116(B4). https://doi.org/10.1029/2010JB008033

Rutter EH (1972) The effects of strain-rate changes on the strength and ductility of Solnhofen limestone at low temperatures and confining pressures. Int J Rock Mech Min Sci Geomech Abstracts 9(2):183–189. https://doi.org/10.1016/0148-9062(72)90020-4

Rutter EH, Mainprice DH (1978) The effect of water on stress relaxation of faulted and unfaulted sandstone. Pure Appl Geophys 116(4):634–654. https://doi.org/10.1007/BF00876530

Rutter EH, Maddock RH, Hall SH, White SH (1986) Comparative microstructures of natural and experimentally produced clay-bearing fault gouges. Pure Appl Geophys 124(1):3–30. https://doi.org/10.1007/BF00875717

Rybacki E, Reinicke A, Meier T, Makasi M, Dresen G (2015) What controls the mechanical properties of shale rocks?—Part I: strength and Young's modulus. J Petrol Sci Eng 135:702–722. https://doi.org/10.1016/j.petrol.2015.10.028

Saffer DM, Marone C (2003) Comparison of smectite- and illite-rich gouge frictional properties: application to the updip limit of the seismogenic zone along subduction megathrusts. Earth Planet Sci Lett 215(1–2):219–235. https://doi.org/10.1016/s0012-821x(03)00424-2

Sari M, Sarout J, Poulet T, Dautriat J, Veveakis M (2022) The brittle-ductile transition and the formation of compaction bands in the savonnières limestone: impact of the stress and pore fluid. Rock Mech Rock Eng 55(11):6541–6553. https://doi.org/10.1007/s00603-022-02963-z

Sarout J, Guéguen Y (2008) Anisotropy of elastic wave velocities in deformed shales: Part 1—Experimental results. Geophysics 73(5):D75–D89. https://doi.org/10.1190/1.2952744

Sarout J, Molez L, Guéguen Y, Hoteit N (2007) Shale dynamic properties and anisotropy under triaxial loading: experimental and theoretical investigations. Phys Chem Earth Parts a/b/c 32(8):896–906. https://doi.org/10.1016/j.pce.2006.01.007

Sarout J, Delle Piane C, Nadri D, Esteban L, Dewhurst DN (2014a) A robust experimental determination of Thomsen's δ parameter. Geophysics 80(1):A19–A24. https://doi.org/10.1190/geo2014-0391.1

Sarout J, Esteban L, Delle Piane C, Maney B, Dewhurst DN (2014b) Elastic anisotropy of Opalinus Clay under variable saturation

and triaxial stress. Geophys J Int 198(3):1662–1682. https://doi.org/10.1093/gji/ggu231
Sayers CM (1999) Stress-dependent seismic anisotropy of shales. Geophysics 64(1):93–98. https://doi.org/10.1190/1.1444535
Sayers CM (2013) The effect of anisotropy on the Young's moduli and Poisson's ratios of shales. Geophys Prospect 61(2):416–426. https://doi.org/10.1111/j.1365-2478.2012.01130.x
Sayers CM, den Boer LD (2016) The elastic anisotropy of clay minerals. Geophysics 81(5):C193–C203. https://doi.org/10.1190/geo2016-0005.1
Sayers CM, Kachanov M (1995) Microcrack-induced elastic wave anisotropy of brittle rocks. J Geophys Res 100(B3):4149–4156. https://doi.org/10.1029/94JB03134
Schmitt L, Forsans T, Santarelli FJ (1994) Shale testing and capillary phenomena. Int J Rock Mech Min Sci Geomech Abstracts 31(5):411–427. https://doi.org/10.1016/0148-9062(94)90145-7
Schoenberg M, Helbig K (1997) Orthorhombic media: Modeling elastic wave behavior in a vertically fractured earth. Geophysics 62(6):1954–1974. https://doi.org/10.1190/1.1444297
Scholz CH (2019) The Mechanics of Earthquakes and Faulting, 3rd edn. Cambridge University Press, Cambridge
Scholz CH (1968) Microfracturing and the inelastic deformation of rock in compression. J Geophys Res (1896–1977), 73(4): 1417–1432. https://doi.org/10.1029/JB073i004p01417
Scholz CH (1972) Static fatigue of quartz. J Geophys Res (1896–1977), 77(11): 2104–2114. https://doi.org/10.1029/JB077i011p02104
Schuster K, Amann F, Yong S, Bossart P, Connolly P (2017) High-resolution mini-seismic methods applied in the Mont Terri rock laboratory (Switzerland). Swiss J Geosci 110(1):213–231. https://doi.org/10.1007/s00015-016-0241-4
Schuster V, Rybacki E, Bonnelye A, Herrmann J, Schleicher AM, Dresen G (2021) Experimental deformation of opalinus clay at elevated temperature and pressure conditions: mechanical properties and the influence of Rock Fabric. Rock Mech Rock Eng 54(8):4009–4039. https://doi.org/10.1007/s00603-021-02474-3
Schuster V, Rybacki E, Bonnelye A, Kwiatek G, Schleicher AM, Dresen G (2023) Strain partitioning and frictional behavior of opalinus clay during fault reactivation. Rock Mech Rock Eng 56(3):2065–2101. https://doi.org/10.1007/s00603-022-03129-7
Schuster V, Rybacki E, Bonnelye A, Dresen G (2022) Authors' reply to the discussion by Crisci et al. (2021) on "Experimental deformation of Opalinus clay at elevated temperature and pressure conditions mechanical properties and the influence of rock fabric". Rock Mech Rock Eng 55(1):467–469. https://doi.org/10.1007/s00603-021-02675-w
Siegesmund S, Popp T, Kaufhold A, Dohrmann R, Grasle W, Hinkes R, Schulte-Kortnack D (2014) Seismic and mechanical properties of Opalinus Clay: comparison between sandy and shaly facies from Mont Terri (Switzerland). Environ Earth Sci 71(8):3737–3749. https://doi.org/10.1007/s12665-013-2768-2
Skempton AW (1954) The pore-pressure coefficients A and B. Geotechnique 4(4):143–147. https://doi.org/10.1680/geot.1954.4.4.143
Soe AKK, Osada M, Takahashi M, Sasaki T (2009) Characterization of drying-induced deformation behaviour of Opalinus Clay and tuff in no-stress regime. Environ Geol 58(6):1215–1225. https://doi.org/10.1007/s00254-008-1616-2
Sone H, Zoback MD (2013a) Mechanical properties of shale-gas reservoir rocks—Part 1: Static and dynamic elastic properties and anisotropy. Geophysics 78(5):D381–D392. https://doi.org/10.1190/geo2013-0050.1
Sone H, Zoback MD (2013b) Mechanical properties of shale-gas reservoir rocks—Part 2: Ductile creep, brittle strength, and their relation to the elastic modulus. Geophysics 78(5):D393–D402. https://doi.org/10.1190/geo2013-0051.1
Stanchits S, Vinciguerra S, Dresen G (2006) Ultrasonic Velocities, Acoustic Emission Characteristics and Crack Damage of Basalt and Granite. Pure Appl Geophys 163(5):975–994. https://doi.org/10.1007/s00024-006-0059-5
Stanchits S, Mayr S, Shapiro S, Dresen G (2011) Fracturing of porous rock induced by fluid injection. Tectonophysics 503(1):129–145. https://doi.org/10.1016/j.tecto.2010.09.022
Terzaghi KV (1936) The shearing resistance of saturated soils and the angle between the planes of shear. Paper presented at the First international conference on soil Mechanics 1936
Thompson BD, Young RP, Lockner DA (2009) Premonitory acoustic emissions and stick-slip in natural and smooth-faulted Westerly granite. J Geophys Res 114(B2). https://doi.org/10.1029/2008JB005753
Thomsen L (1986) Weak elastic anisotropy. Geophysics 51(10):1954–1966. https://doi.org/10.1190/1.1442051
Thury MF, Bossart PJ (1999) Mont terri rock laboratory: results of the hydrogeological, geochemical and geotechnical experiments performed in 1996 and 1997 (Vol. Geologischer Bericht Nr. 23): Landeshydrologie und-geologie.
Tremosa J, Arcos D, Matray JM, Bensenouci F, Gaucher EC, Tournassat C, Hadi J (2012) Geochemical characterization and modelling of the Toarcian/Domerian porewater at the Tournemire underground research laboratory. Appl Geochem 27(7):1417–1431. https://doi.org/10.1016/j.apgeochem.2012.01.005
Valès F, Nguyen Minh D, Gharbi H, Rejeb A (2004) Experimental study of the influence of the degree of saturation on physical and mechanical properties in Tournemire shale (France). Appl Clay Sci 26(1):197–207
Van Eeckhout EM (1976) The mechanisms of strength reduction due to moisture in coal mine shales. Int J Rock Mech Min Sci Geomech Abstracts 13(2):61–67. https://doi.org/10.1016/0148-9062(76)90705-1
Vanorio T, Mukerji T, Mavko G (2008) Emerging methodologies to characterize the rock physics properties of organic-rich shales. Lead Edge 27(6):780–787. https://doi.org/10.1190/1.2944163
Vernik L, Liu X (1997) Velocity anisotropy in shales: a petrophysical study. Geophysics 62(2):521–532. https://doi.org/10.1190/1.1444162
Vernik L, Nur A (1992) Ultrasonic velocity and anisotropy of hydrocarbon source rocks. Geophysics 57(5):727–735. https://doi.org/10.1190/1.1443286
Volpe G, Pozzi G, Collettini C (2022) Y-B-P-R or S-C-C′? Suggestion for the nomenclature of experimental brittle fault fabric in phyllosilicate-granular mixtures. J Struct Geol 165:104743. https://doi.org/10.1016/j.jsg.2022.104743
Wang Z (2002) Seismic anisotropy in sedimentary rocks, part 2: Laboratory data. Geophysics 67(5):1423–1440. https://doi.org/10.1190/1.1512743
Wawerzinek B, Lüth S, Esefelder R, Giese R, Krawczyk CM (2022) Performance of high-resolution impact and vibration sources for underground seismic exploration of clay formations at the scale of a rock laboratory. Geophys J Int 231(3):1750–1766. https://doi.org/10.1093/gji/ggac283
Wenk HR, Voltolini M, Mazurek M, Van Loon LR, Vinsot A (2008) Preferred orientations and anisotropy in shales: Callovo-Oxfordian shale (France) and opalinus clay (Switzerland). Clays Clay Miner 56(3):285–306. https://doi.org/10.1346/Ccmn.2008.0560301
Wenning QC, Madonna C, Zappone A, Grab M, Rinaldi AP, Plötze M, Wiemer S (2021) Shale fault zone structure and stress dependent anisotropic permeability and seismic velocity properties (Opalinus Clay, Switzerland). J Struct Geol 144: 104273. https://doi.org/10.1016/j.jsg.2020.104273
Wild KM, Amann F (2018) Experimental study of the hydro-mechanical response of Opalinus Clay - Part 1: Pore pressure response

and effective geomechanical properties under consideration of confinement and anisotropy. Eng Geol 237:32–41. https://doi.org/10.1016/j.enggeo.2018.02.012

Wild KM, Wymann LP, Zimmer S, Thoeny R, Amann F (2015) Water retention characteristics and state-dependent mechanical and petro-physical properties of a clay shale. Rock Mech Rock Eng 48(2):427–439. https://doi.org/10.1007/s00603-014-0565-1

Williams M, Ziegler M, Schennen S, Loew S (2022) Evolution of excavation damaged zones in Opalinus Clay shale inferred from seismic investigations. Eng Geol 299:106528. https://doi.org/10.1016/j.enggeo.2022.106528

Winhausen L, Khaledi K, Jalali M, Urai JL, Amann F (2022) Failure mode transition in Opalinus Clay: a hydro-mechanical and microstructural perspective. Solid Earth 13(5):901–915. https://doi.org/10.5194/se-13-901-2022

Winhausen L, Khaledi K, Jalali M, Bretthauer M, Amann F (2023) The Anisotropic behavior of a clay shale: strength, hydro-mechanical couplings and failure processes. J Geophys Res 128(11): e2023JB027382. https://doi.org/10.1029/2023JB027382

Wong T-F, Baud P (2012) The brittle-ductile transition in porous rock: a review. J Struct Geol 44:25–53. https://doi.org/10.1016/j.jsg.2012.07.010

Wong T-F, Szeto H, Zhang J (1992) Effect of loading path and porosity on the failure mode of porous rocks. Appl Mech Rev 45(8):281–293. https://doi.org/10.1115/1.3119759

Wong T-F, David C, Zhu W (1997) The transition from brittle faulting to cataclastic flow in porous sandstones: Mechanical deformation. J Geophys Res 102(B2):3009–3025. https://doi.org/10.1029/96JB03281

Yurikov A, Lebedev M, Pervukhina M, Gurevich B (2019) Water retention effects on elastic properties of Opalinus shale. Geophys Prospect 67(4):984–996. https://doi.org/10.1111/1365-2478.12673

Zang A, Christian Wagner F, Stanchits S, Dresen G, Andresen R, Haidekker MA (1998) Source analysis of acoustic emissions in Aue granite cores under symmetric and asymmetric compressive loads. Geophys J Int 135(3):1113–1130. https://doi.org/10.1046/j.1365-246X.1998.00706.x

Zappone A, Rinaldi AP, Grab M, Wenning QC, Roques C, Madonna C, Wiemer S (2021) Fault sealing and caprock integrity for CO2 storage: an in situ injection experiment. Solid Earth 12(2):319–343. https://doi.org/10.5194/se-12-319-2021

Zega Z, Zhu W (2023) Stabilizing effect of high pore fluid pressure on fault growth during drained deformation. J Geophys Res 128(8): e2023JB026536. https://doi.org/10.1029/2023JB026536

Zhang C-L (2017) Examination of effective stress in clay rock. J Rock Mech Geotech Eng 9(3):479–489. https://doi.org/10.1016/j.jrmge.2016.07.008

Zhang C-L, Talandier J (2022) Self-sealing of fractures in indurated claystones measured by water and gas flow. J Rock Mech Geotech Eng. https://doi.org/10.1016/j.jrmge.2022.01.014

Zhang F, Xie SY, Hu DW, Shao JF, Gatmiri B (2012) Effect of water content and structural anisotropy on mechanical property of claystone. Appl Clay Sci 69:79–86. https://doi.org/10.1016/j.clay.2012.09.024

Zhang C-L, Armand G, Conil N, Laurich B (2019) Investigation on anisotropy of mechanical properties of Callovo-Oxfordian claystone. Eng Geol 251:128–145. https://doi.org/10.1016/j.enggeo.2019.02.008

Zou C, Dong D, Wang S, Li J, Li X, Wang Y, Cheng K (2010) Geological characteristics and resource potential of shale gas in China. Petroleum Exploration and Development, 37(6): 641–653. https://doi.org/10.1016/S1876-3804(11)60001-3